A Multi-Parametric Microwave-Optical Biomolecular Sensor

Luya Zhang
Ali Niknejad

Electrical Engineering and Computer Sciences
University of California at Berkeley

December 1, 2019

Acknowledgement

A Multi-Parametric Microwave-Optical Biomolecular Sensor

by Luya Zhang

Research Project

Submitted to the Department of Electrical Engineering and Computer Sciences, University of California at Berkeley, in partial satisfaction of the requirements for the degree of **Master of Science, Plan II**.

Approval for the Report and Comprehensive Examination:

Committee:
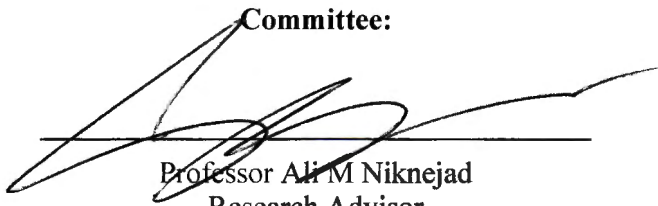
Professor Ali M Niknejad
Research Advisor

12/11/18

(Date)

* * * * * * *

Professor Chunlei Liu
Second Reader

12/11/18

(Date)

A Multi-Parametric Microwave-Optical Biomolecular Sensor

by

Luya Zhang

A thesis submitted in partial satisfaction of the

requirements for the degree of

Master of Science, Plan II

in

Electrical Engineering and Computer Sciences

in the

Graduate Division

of the

University of California, Berkeley

Committee in charge:

Professor Ali M. Niknejad, Chair
Professor Chunlei Liu

Fall 2018

The thesis of Luya Zhang, titled A Multi-Parametric Microwave-Optical Biomolecular Sensor, is approved:

Chair _____   Date _____

_____   Date _____

University of California, Berkeley

IEEE Copyright Notice

Abstract

A Multi-Parametric Microwave-Optical Biomolecular Sensor

by

Luya Zhang

Master of Science, Plan II in Electrical Engineering and Computer Sciences

University of California, Berkeley

Professor Ali M. Niknejad, Chair

Multi-parameter real-time profiling of biological and chemical molecules and reactions provides important insights into their mechanisms of action, which serves as the first step to further advance in bioscience and bioengineering. Compared with bulky laboratory solutions, CMOS technologies allow massive integration of different sensor modalities, including optical, electrical, ultrasound, mechanical, etc., onto a single mm-sized sensing platform. This lab-on-CMOS concept is advantageous in probing the biomolecular processes with high sensitivity and specificity in a quantitative way. This work explores the design of a hybrid microwave and optical biomolecular sensor in 28nm CMOS process. The microwave sensing unit is a superharmonic coupled QVCO (quadrature voltage controlled oscillator) for permittivity detection which achieves label/reference-free 5.4ppm 8-hour stability. The optical sensing unit is an SPAD (single photon avalanche diode) array for photon counting and fluorescent lifetime measurements. Experiments on enzyme denaturation under thermal and chemical stress are performed to demonstrate the benefits of this multi-parametric lab-on-CMOS sensing solution.

Contents

List of Figures

List of Tables

Acknowledgments

Chapter 1

Introduction

1.1 Motivation

Quantitative and specific monitoring of biomolecular reactions has numerous clinical and research applications, such as immunodiagnostics, drug discovery and cellular phenotyping. For example, characterization and understanding of the mechanism of drug action is the primary step for the scientific progress towards a more comprehensive and realistic therapeutic usage of a certain drug. Due to the extreme complexity of biomolecular interactions, it is crucial to implement a sensing system which can detect different physical signals and thereby differentiate different target biomolecules. In reality, each sensing method has its own strength and weakness and cannot capture all information, which necessitates a multiplexed sensing scheme for better accuracy and sensitivity.

A typical biosensing system consists of a bioreceptor and a biotransducer. The bioreceptor is designed to interact with a specific analyte of interest, and produce a measurable signal to the biotransducer. The most common example is the antibody-antigen interaction used in immunodiagnostics, where a successful binding will produce a sensible signal such as light emission or PH changes. The biotransducer transforms the received signal to a different form which is easier to measure and quantify, usually an electrical signal. Multiplexed sensing involves engineering innovations in both bioreceptor design (mostly in the field of biological engineering) and biotransducer design (mostly in the field of electrical engineering), which is the focus of this work.

Compared with bulky laboratory equipment, monolithic integration of multiparametric biotransducers on a single small CMOS chip is advantageous in the sense that it enables real-time truly-parallel (not time-interleaved) monitoring of bio-reactions with minimal amount of bio-samples required. A multiparametric imager can also be realized by converting a single sensor node into an array, which allows studying the heterogeneity in biological systems.

Recently, a quad-modality biosensor[2] was demonstrated for cellular assays, which detects sub-MHz impedance, voltage and optical opacity in a standard CMOS process. How-

ever, biomolecular reaction monitoring requires methods with high sensitivity and long-term stability to resolve weak response from complicated bio-mixtures over multi-hour experiments. The work in [2], on the other hand, exploits the high sensitivity and selectivity of cell-based biorecepters to compensate the suboptimal performance of CMOS sensors, which is undesirable. Although much progress has been made in developing high sensitivity CMOS biochips (dielectric[3], magnetic[4], fluorescence[5]), most only support single sensing modality. As for long-term stability, existing designs rely on a replica reference[3, 6] or specific detection labels[4] for compensation, which will cease to have effect when such an identical replica or the specific label is not available.

In order to address these challenges, a hybrid microwave and optical biomolecular sensor is presented here. The microwave sensor detects complex permittivity changes produced by the biomolecular reactions in a frequency range of 37.5GHz to 45.1GHz. Sensing at microwave frequencies (above GHz) bypasses the electrical double layer of the ionic bio-medium and probes the intrinsic biomolecular properties. The 40GHz frequency range is selected to minimize the artifacts caused by biological water Debye relaxation [7, Table I] (18GHz at $25\,°C-30$GHz at $40\,°C$) when performing material frequency-dependent dispersion measurements. The core sensing element is a superharmonic coupled quadrature VCO (QVCO). Changes of complex permittivity are translated into the QVCO frequency shifts and converted to quadrature error signals to obviate power-hungry mm-wave frequency dividers. With a novel tank-perturbation based noise-drift-cancellation readout scheme, 5.4ppm 8-hour long-term stability is achieved with no replica reference or detection labels required. The optical sensing element is an array of single photon avalanche diodes (SPADs), which detects both photon number and photon emission time. With a pulsed laser, fluorescent lifetime (FLT) can be measured for further biomolecular classification.

1.2   Thesis Organization

In Chapter 2, the design and implementation of the QVCO-based permittivity sensor element is demonstrated. It starts with a literature survey and comparison of existing oscillator-based reactance sensor architectures. A new superharmonic coupled QVCO sensing front-end is then presented, accompanied with a thorough circuit analysis of its working mechanism. As for signal readout, a novel tank-perturbation based noise-cancellation readout scheme is proposed to improve label-and-reference-freel long-term stability. In Chapter 3, the design and implementation of the SPAD-based optical sensor element is given. This chapter begins with the benefits and implementation challenges of SPADs in sub-100nm CMOS processes, and then proceeds to the operation mechanism and important figures of merit of SPADs. Next, the SPAD design details are presented on the device level and circuit level. Device performance measurements and comparisons with prior works are included as well. In Chapter 4, both single-modality and dual-modality sensing measurements are performed and results are shown. Chapter 5 concludes this work.

Chapter 2

Microwave Permittivity Sensor

2.1   Oscillator-based Permittivity Sensor

Oscillators are widely used for reactance (permittivity or permeability) sensing since the change in reactance can be directly translated into the change in the oscillator natural frequency for easy readout [3, 8–10]. As shown in Fig. 2.1, there are in general two different modalities to detect the shift in the oscillator natural frequency. In Fig. 2.1(a), the sensing front-end is simply a stand-alone free-running oscillator whose oscillation frequency is digitized by counting the number of the toggling edge over a predefined time period. An additional reference oscillator is usually used as reference for flicker noise and low frequency drift cancellation. In Fig. 2.1(b), the sensing oscillator is injection-locked to a signal source and runs at a fixed frequency. The change in its natural frequency is thereby converted into a phase shift and compared with a reference oscillator (also injection-locked to the same signal source) with a phase detector (PD). In this section, the operation mechanism and sensitivity resolution of these two different sensing modalities are reviewed, and the strength and limits in each design are analyzed.

Free-running Oscillator and Direct Frequency Counting

When a free-running oscillator is used as a reactance sensor, the frequency shift is detected by counting against a precise external clock reference. Therefore, the sensitivity limit is determined by the accumulated jitter over the counting window, which is eventually set by the correlated low frequency noise/drift given a sufficiently long integration time.

As shown in Fig. 2.1(a), two identical LC tanks are implemented with one of which serves as the sensing element and the other as reference. The two LC tanks share the same regenerative cross-coupled stage through a multiplexer, so that the low frequency flicker noise and slow drift contributed by the cross-coupled pair are suppressed in a correlated double counting (CDC) fashion[1]. With CDC, the minimum resolvable frequency shift, i.e., the
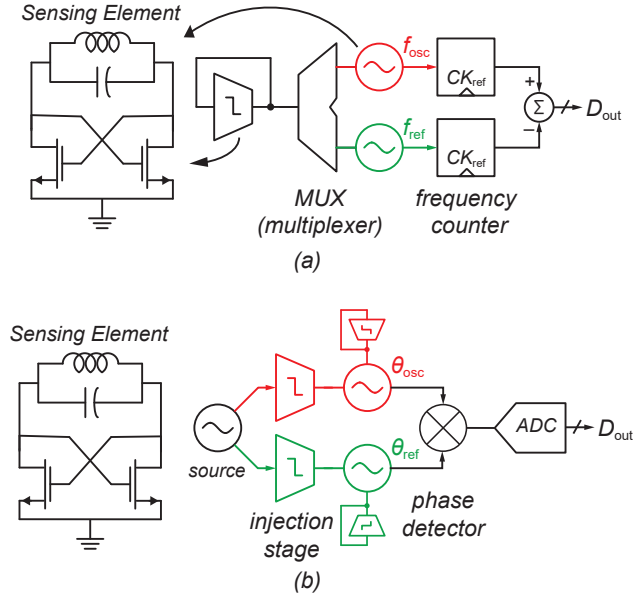
Figure 2.1: Two types of oscillator-based reactance sensors, (a) stand-alone free-running oscillator with a frequency counter and (b) unidirectional-injection-locked oscillator with a phase detector.

residue frequency noise, is given by

$$\left(\frac{\Delta\omega_{n,rms}}{\omega_0}\right)^2 = \frac{1}{\pi\omega_0^2\tau^2}\int_0^\infty S_\phi(\omega)|H_{\mathrm{LPF}}(\omega)|^2 d\omega \tag{2.1}$$

where $S_\phi(\omega)$ is the SSB phase noise of the oscillator and $H_{\mathrm{LPF}}(\omega)$ is the noise filtering applied to the sensor through CDC[1]. The filtering effect is given by

$$|H_{\mathrm{LPF}}(\omega)|^2 = 16\sin^4\left(\frac{\omega\tau}{2}\right) \tag{2.2}$$

Assuming the correlated phase noise is dominant, as much as 9.6dB improvement in the sensing sensitivity can be realized through CDC.

However, this CDC scheme requires that the two oscillators operate in a time-interleaved fashion to (1) cancel the flicker noise in the cross-coupled pair and (2) to avoid mutual lock. Besides, in the practical measurement, the frequency counter can experience a non-negligible dead time caused by counter reset, oscillation start-up and die-away, which interrupts the continuous counting. Such interruption adversely affect the effectiveness of the CDC on noise suppression, as shown in Fig. 2.2(b)[1]. Although a higher order interleaving CDC scheme was proposed to sample and cancel the slowly varying $1/f^3$ phase noise at a higher rate to achieve better noise attenuation, there exists an upper limit of the sampling rate which is set by the oscillator start-up/die-away time, a constant proportional to the tank quality
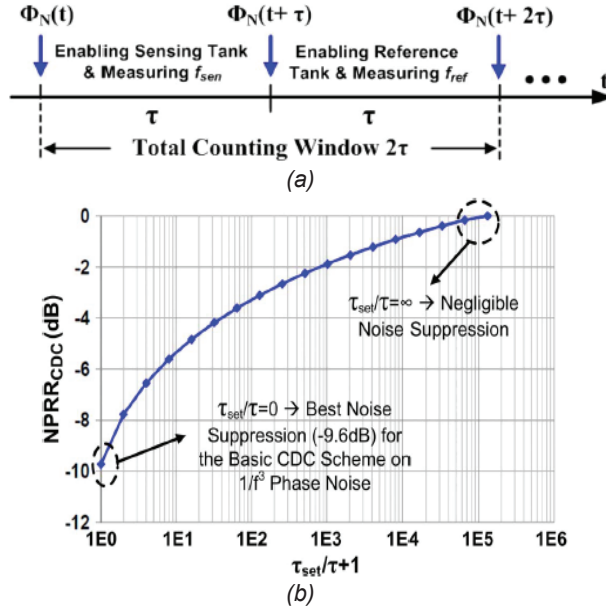
Figure 2.2: Correlated double counting (CDC) to improve sensitivity[1], (a) interleaved frequency counting and (b) sensitivity degeneration due to dead time τ_{set}.

factor Q. Apparently this CDC scheme suffers from a severe trade-off between flicker noise attenuation and power consumption/thermal noise performance. It is also worth mentioning that the sampling behavior also causes broadband noise folding, which yields a kT/C noise, although it is hard to model the effective C.

Unidirectional-Injection-locked Oscillator and Phase Detection

As shown in Fig. 2.1(b), the operation of unidirectional-injection-lock based reactance sensing can be described as follows[3]. Two identical oscillators (one sensing and the other reference) are unidirectionally locked to a third oscillator and ideally present identical phase at the input of the phase detector (PD). When the sensing oscillator is loaded with some samples, the change in its natural frequency will produce a phase shift at its output since its oscillation frequency remains unchanged due to injection locking. The phase detector sees the phase shift and convert it into a voltage to be digitized by the ADC.

Fig. 2.3 illustrates how the natural frequency change $\Delta\omega$ is translated into the phase shift θ in a two-step fashion. First of all, $\Delta\omega$ leads to off-resonance injection locking, which forces a phase difference α between the tank voltage (also I_{osc}) and tank current I_{tank}. Such phase difference is then amplified to a output phase shift θ. The transfer function from $\Delta\omega$ to θ can be derived as

$$\theta \simeq \frac{\Delta\omega}{\omega}(2Q)(1 + \frac{1}{I_{\text{inj}}/I_{\text{osc}}}) \tag{2.3}$$
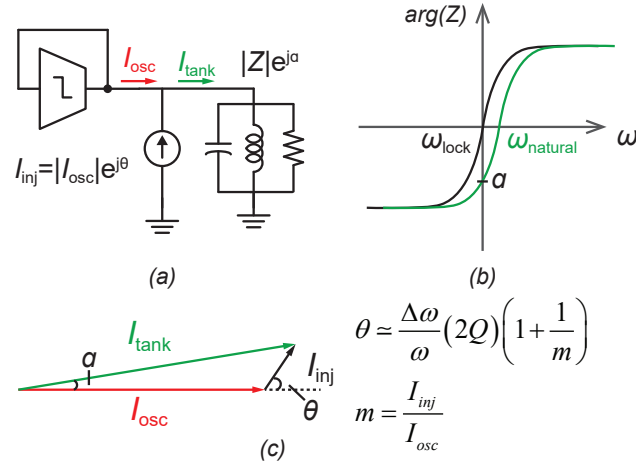
Figure 2.3: Unidirectional-injection-locked-oscillator (U-ILO) based reactance sensing, (a) U-ILO model, (b) sensor transfer curve and (c) steady-state phasor diagram.

There are several advantages associated with phase readout compared with frequency readout. Since most materials have a frequency dependent permittivity and permeability, working at a fixed frequency allows a clearer definition of the sensor output as well as an unambiguous comparison between different materials. Besides, since both the sensing and reference oscillator operate in a continuous mode with no dead time penalty, the highest possible common-mode rejection could be achieved. Moreover, as Eq. (2.3) implies, there exists an inherent amplification factor $2Q(1 + 1/m)$ (where $m = I_{\text{inj}}/I_{\text{osc}}$ is the relative injection strength) in the phase readout scheme, which improves the sensor performance further.

The noise and sensitivity of this injection-lock based sensor can be analyzed using *Adler's Equation*. Phase noise is contributed by (1) the external excitation oscillator plus injection devices and (2) the sensing/reference oscillator itself. Assume an oscillator with a natural frequency of ω_0 is pulled by $I_{\text{inj}}e^{\phi_{\text{inj}}}$ to produce a time-varying phase $\phi(t)$, then the *Adler's Equation*[11] requires

$$\frac{d\phi}{dt} = \omega_0 + \frac{\omega_0}{2Q}\frac{\pi}{4}\frac{I_{\text{inj}}}{I}\sin(\phi_{\text{inj}} - \phi) \tag{2.4}$$

Under lock $\phi = \omega_{\text{inj}}t$ and $\phi_{\text{inj}} = \omega_{\text{inj}}t + \theta$. Suppose that ϕ is disturbed as $\hat{\phi} = \omega_{\text{inj}}t + \phi_n$ due to the phase noise from the excitation source $\hat{\phi}_{\text{inj}} = \omega_{\text{inj}}t + \theta + \phi_{\text{inj,n}}$. Substituting in Eq. (2.4) yields

$$\frac{d\phi_n}{dt} = \frac{\omega_0}{2Q}\frac{\pi}{4}\frac{I_{\text{inj}}}{I}\cos(\theta)(\phi_{\text{inj,n}} - \phi_n) \tag{2.5}$$

Transforming to s domain shows a low pass filter effect $(\theta_n(0^-) = 0)$

$$H_{\text{LPF}}(s) = \frac{\Theta_n(s)}{\Theta_{\text{INJ,n}}(s)} = \frac{\omega_{\text{LR}}\cos(\theta)}{s + \omega_{\text{LR}}\cos(\theta)} \tag{2.6}$$

where $\omega_{\text{LR}} = \frac{\omega_0}{2Q}\frac{\pi}{4}\frac{I_{\text{inj}}}{I}$ is the injection locking range.

On the other hand, the phase noise from the oscillator itself will experience a high pass filtering process. Again, assume $\hat{\phi} = \omega_{\text{inj}}t + \phi_n$ when perturbed by $\hat{\omega}_0 = \omega_0 + d\psi_n/dt$. Only close-in phase noise is of concern thus $d\psi_n/dt \ll \omega_0$. Substituting in Eq. (2.4) yields

$$\frac{d\phi_n}{dt} = \frac{d\psi_n}{dt} + \frac{d\psi_n/dt}{2Q}\frac{\pi}{4}\frac{I_{\text{inj}}}{I}\sin(\theta - \phi_n) - \frac{\omega_0}{2Q}\frac{\pi}{4}\frac{I_{\text{inj}}}{I}\cos(\theta)(\phi_n) \tag{2.7}$$

Further simplification gives

$$\frac{d\phi_n}{dt} = \frac{d\psi_n}{dt}\left(1 + \frac{\omega_{\text{LR}}}{\omega_0}\sin(\theta)\right) - \omega_{\text{LR}}\cos(\theta)(\phi_n) \tag{2.8}$$

With s-transformation,

$$H_{\text{HPF}}(s) = \frac{\Theta_n(s)}{\Psi_n(s)} = \frac{s(1 + \frac{\omega_{\text{LR}}}{\omega_0}\sin(\theta))}{s + \omega_{\text{LR}}\cos(\theta)} \simeq \frac{s}{s + \omega_{\text{LR}}\cos(\theta)} \tag{2.9}$$

Therefore the total output phase noise can be expressed as

$$\begin{aligned}\Theta_n(s) &= H_{\text{LPF}}(s)\Theta_{\text{INJ,n}}(s) + H_{\text{HPF}}(s)\Psi_n(s)\\ &= \frac{\omega_{\text{LR}}\cos(\theta)}{s + \omega_{\text{LR}}\cos(\theta)}\Theta_{\text{INJ,n}}(s) + \frac{s}{s + \omega_{\text{LR}}\cos(\theta)}\Psi_n(s)\end{aligned} \tag{2.10}$$

where $\theta = 0$ for the reference oscillator and $\theta = \frac{\Delta\omega}{\omega}(2Q)(1 + 1/m)$ for the sensing oscillator. Assume $S_{\phi,\text{INJ}}$, $S_{\phi,\text{SEN}}$ and $S_{\phi,\text{REF}}$ represent the SSB noise of the external excitation source (including noise from injection current due to AM-PM conversion), the sensing oscillator and the reference oscillator, respectively. The output phase noise can be calculated as

$$\begin{aligned}S_{\text{out,n}} = {}&S_{\phi,\text{INJ}}|H_{\text{LPF},\theta=\theta_s}(s) - H_{\text{LPF},\theta=0}(s)|^2 +\\ &S_{\phi,\text{SEN}}|H_{\text{HPF},\theta=\theta_s}(s)|^2 + S_{\phi,\text{REF}}|H_{\text{HPF},\theta=0}(s)|^2\end{aligned} \tag{2.11}$$

The minimal detectable frequency resolution normalized by ω_0 is derived by dividing Eq. (2.11) by Eq. (2.3)

$$\left(\frac{\Delta\omega}{\omega_0}\right)^2\Big|_{\text{RMS,n}} = \frac{\int_{-\infty}^{+\infty} S_{\text{out,n}}d\omega}{(2Q(1 + 1/m))^2} \simeq \int_{-\infty}^{+\infty}(S_{\phi,\text{SEN}} + S_{\phi,\text{REF}})\frac{\omega^2}{\omega_0^2}\frac{\omega_{\text{LR}}^2}{\omega^2 + \omega_{\text{LR}}^2}d\omega \tag{2.12}$$

Several conclusions can be drawn here:

1. An optimal design sets the locking range ω_{LR}, which is also the 3dB frequency of $H_{\text{LPF}}(s)$ and $H_{\text{HPF}}(s)$, to be above the flicker phase noise corner of all three oscillators, so that the correlated $S_{\phi,\text{INJ}}$ gets canceled and the uncorrelated $S_{\phi,\text{SEN}}$ and $S_{\phi,\text{REF}}$ flicker parts are attenuated.

2. Residual noise includes (1) uncorrelated injection device noise, (2) reference/sensing oscillator phase noise (above ω_{LR}) and (3) excitation source noise leaking due to $H_{\mathrm{LPF}}(s)$ path mismatch. They are mostly white with careful design and therefore can be reduced with averaging.

3. Eq.(2.12) implies a smaller ω_{LR} (a higher tank Q or weaker injection strength m) helps to reduce the frequency noise floor, which sets the lower bound of ω_{LR}. The claim made in [3] that the noise floor is independent of m is incorrect because it uses a wrong $H_{\mathrm{HPF}}(s)$. The measurement in [3, Fig.18(b)] agrees with the conclusion here.

4. All the derivations up to this point ignores the multiplicative noise contributed by the gain factor in Eq.(2.3). It will lead to severe performance degradation if it's not white. Variable separation with logarithmic operation can convert it into additive noise and may help in noise reduction.

Mutually-Locked Oscillator and Phase Detection

Based on the discussion above, two mutually-locked oscillators should be the optimal sensor configuration since it (a) allows sensing at a fixed frequency via injection locking, (b) correlates noise better for cancellation and (c) reduces power consumption. Moreover, it is of particular interest in the scope of this project to build sensing oscillators at mm-wave frequencies because it allows the study of material dielectric properties at such high frequencies and it makes it easier to tune ω_{LR} higher than flicker corner since it scales linearly with ω_0.

Therefore, the use of two mm-wave quadrature locked oscillators (QVCO) as reactance sensing is explored in this chapter. Instead of in-phase locking, quadrature locking is selected since it produces a monotonic high-gain output with a self-mixing phase detector ($\sin(\theta)$ for quad-lock while $\cos(\theta)$ for in-phase-lock, where θ is the phase shift). Section 2.2 discusses the design details of the proposed QVCO structure and Section 2.3 describes a novel sensor readout scheme and provides a sensitivity analysis.

2.2   Sensor Core Design

Popular methods of generating quadrature signals include using poly-phase filters or quadrature hybrid, divide-by-2 frequency dividers, and coupled VCOs. At mm-wave frequencies, quadrature coupled oscillators (QVCO) are attractive due to their superior power and area efficiency. The original QVCO proposed in [12] used a parallel coupling scheme which suffered from poor phase noise performance and severe trade-off between quadrature accuracy and phase noise due to off-resonance injection locking. Series coupling [13] showed an improved phase noise and phase accuracy performance at the expense of increased voltage headroom. Moreover, coupling networks that are directly connected to the IQ differential ports are extensively studied to achieve better phase noise and phase accuracy through in-

phase-injection-locking[14, 15]. However, these coupling devices add extra parasitics and loss to the LC tank which impairs both tuning range and tank quality factor.

Instead of coupling through fundamental components, quadrature locking can also be achieved by enforcing a 180° phase difference between the two 2nd harmonics extracted from IQ oscillator common-mode nodes, i.e., by superharmonic (S-H) coupling. For example, [16] used an inverting transformer to resonate out the tail capacitor at $2\omega_0$ and to ensure quadrature lock at ω_0 (Fig. 2.4(b)), and [17] used a capacitive-cross-coupled pair to generate phase quadrature (Fig. 2.4(c)). Theoretically speaking, no significant phase noise penalty should occur using superharmonic coupling as it is inherently able to inject in-phase components at the fundamental frequency. Moreover, locking range and tank Q remain intact. Despite these benefits, superharmonic coupling is predominantly used in sub-10GHz CMOS QVCOs with only moderate phase accuracy. In addition, the mechanism of how a superharmonic network ensures quadrature lock (i.e., ensures a 180° phase difference between the coupled 2nd harmonics) has not been well identified yet.
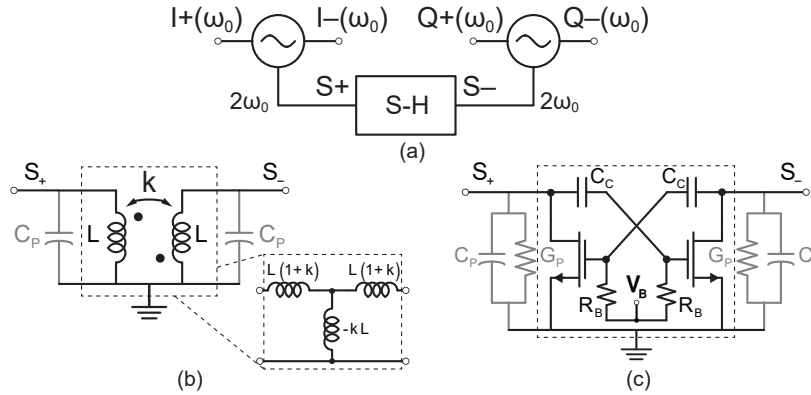
Figure 2.4: (a)Two identical VCOs locked through superharmonic (S-H) coupling network, (b) a transformer based and (c) a capacitive-cross-coupled pair based S-H coupling network.

Here it will be pointed out that the superharmonic coupling network shapes the oscillator loop gain based on the phase difference between the two coupled oscillators. Quadrature mode is selected by maximizing the loop gain at 90° phase difference only. In this Section, a concept of effective negative G_m considering 2nd harmonic is developed to show that the loop gain shaping is realized by stimulating an oscillator-phase-offset-dependent impedance at the two coupled nodes ($S_{+,-}$ in Fig. 2.4(a)). Based on the analysis, a new superharmonic coupling network, suitable for mm-wave QVCOs, is proposed with low phase error and no extra headroom requirement. More importantly, the proposed coupling network can improve quadrature accuracy against oscillator mismatch while leaving the LC tank intact.

Effective Negative G_m

Consider the half circuit of a tail-coupled superharmonic QVCO as shown in Fig. 2.5. Z_s represents the total tail impedance, including parasitic capacitance from the oscillator itself and the impedance presented by the coupling network. The oscillator operates in the voltage-limited regime for optimal phase noise performance, therefore in the steady-state the voltage minima at the tail node aligns with the the differential output extrema (maxima and minima) with a fixed phase offset θ ($-\pi/2 < \theta < \pi/2$) caused by the node net reactance[18]. Assume the differential output voltage to be $A_1 cos(\omega_0 t)$, the tail node can be approximated as a sinusoid with a frequency of $2\omega_0$: $A_2 cos(2\omega_0 t + \pi + \theta)$. Considering the 2nd harmonic at the tail node, the current flowing through each transistor can be modeled by:

$$
\begin{aligned}
I_p &= g_1 V_{\text{GS,p}} + g_2 V_{\text{GS,p}}^2 \\
I_n &= g_1 V_{\text{GS,n}} + g_2 V_{\text{GS,n}}^2
\end{aligned}
\tag{2.13}
$$

where

$$
\begin{aligned}
V_{\text{GS,p}} &= V_{\text{OV,dc}} - 0.5 A_1 \cos(\omega_0 t) - A_2 \cos(2\omega_0 t + \pi + \theta) \\
V_{\text{GS,n}} &= V_{\text{OV,dc}} + 0.5 A_1 \cos(\omega_0 t) - A_2 \cos(2\omega_0 t + \pi + \theta)
\end{aligned}
\tag{2.14}
$$

and V_{OV0} is the DC overdrive voltage. The effective negative G_m can be derived as

$$
G_m = \frac{I_{D,\omega_0}}{A_1} = -(g_1 + g_2 A_2 e^{j\theta})
\tag{2.15}
$$

The second term in the G_m expression originates from the 2nd harmonic at the tail node which is down-converted by the cross-coupled pair.
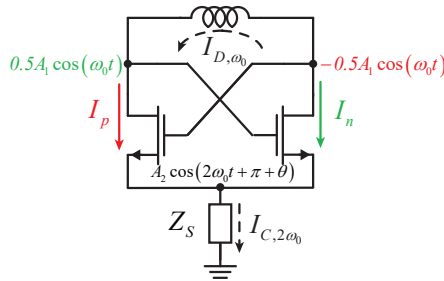
Figure 2.5: Half circuit of a S-H coupled QVCO showing source impedance.

Two conclusions can be drawn from Eq. (2.15) regarding the 2nd harmonic voltage at the tail node. First, increasing its magnitude A_2 increases the effective negative G_m and thereby the oscillator loop gain. Second, reducing the absolute value of the phase angle θ caused by tail reactance also helps to increase the effective G_m and loop gain. Moreover, in-phase injection locking happens at $\theta = 0°$. Since the 2nd harmonic tail current $I_{C,2\omega_0} \simeq \frac{1}{2} g_2 A_1$ is mostly set by A_1, the same conclusions can be directly applied to the tail impedance Z_s.

So far, the relationship between effective G_m (thereby loop gain) and tail impedance Z_s has been established. As will be explained in the following section, in the case of two superharmonic coupled oscillators with a phase offset of ϕ (i.e., $A_1 e^{j\phi/2}$ and $A_1 e^{-j\phi/2}$), the tail impedance Z_s of each oscillator is a function of ϕ, and the magnitude of $Z_s(\phi)$ reaches its maximum under the condition of quadrature locking (i.e., when $\phi = 90°$). As maximizing $\|Z_s(\phi)\|$ (thereby G_m) is equivalent to maximizing oscillator loop gain, it makes the quadrature mode prevail over all the other modes during the oscillator start up, and thereby ensures quadrature locking.

Tail Impedance Analysis

This section derives the analytical expression of the phase-dependent tail impedance $Z_s(\phi)$ for transformer based [16] and capacitive-cross-coupled pair based [17] S-H coupling network. For simplicity, two extreme situations (i) in-phase lock ($\phi = 0°$) and (ii) quadrature lock ($\phi = 90°$) are considered without loss of generality. Based on the derived expressions, it will be shown that these two coupling schemes have poor quadrature accuracy due to mismatch when used in mm-Wave QVCOs, from which a new superharmonic coupling network suitable for mm-wave frequencies will be proposed.

In the case of transformer based S-H coupling network (Fig. 2.4(b)), the tail parasitic capacitance C_P is relatively constant, therefore only transformer inductance value is calculated and compared. Under quadrature lock ($\phi = 90°$), the voltages at the coupled tail nodes $S_{+,-}$ are 180° out of phase and the coupling network is in differential-mode. On the other hand, when the two oscillators are locked in-phase ($\phi = 0°$), $S_+ = S_-$ and the coupling network is in the common-mode. Using the transformer T-model, the effective inductance at $S_{+/-}$ in two modes are

$$
\begin{aligned}
L_{DM,\phi=90°} &= L(1 + k) \\
L_{CM,\phi=0°} &= L(1 - k)
\end{aligned}
\tag{2.16}
$$

The transformer is sized such that at $2\omega_0$ the differential inductance $L_{DM,\phi=90°}$ is in resonance with C_P. Therefore the tail impedance, as well as the effective G_m and loop gain, are maximized at $\phi = 90°$, which makes the two oscillators run in quadrature. Since $L_{CM,\phi=0°} - C_P$ cancellation causes in-phase locking, the ratio $L_{DM,\phi=90°}/L_{CM,\phi=0°} = \frac{1+k}{1-k}$ reflects to what extent the quadrature mode is preferred over other modes. Apparently as ω_0 increases, the transformer inductance L has to drop, which makes it challenging to achieve a high coupling coefficient k. k degradation ($\frac{1+k}{1-k} \to 1$) leads to a reduced preference for quadrature mode, and thereby an increased phase error under oscillator mismatch.

In the case of using a capacitive-cross-coupled pair as coupling network (Fig. 2.4(c)), for now assume low frequency range where the parasitic capacitance C_P is negligible compared with the transconductance of the cross-coupled pair g_m. The tail admittance at $\phi = 90°$ and

$\phi = 0°$ can be expressed as:

$$Y_{DM,\phi=90°} = -g_m + G_P$$
$$Y_{CM,\phi=0°} = g_m + G_P \tag{2.17}$$

where G_P represents the parasitic conductance at the tail node. Note that $Y_{DM,\phi=90°}$ is non-negative because of the transistor non-linearity. The quadrature mode is selected for the same reason. However, when scaling to mm-Wave frequencies, $\omega_0 C_P$ becomes comparable with g_m and eventually erases the impedance contrast established through g_m sign inversion: $Y_{DM,\phi=90°}/Y_{CM,\phi=0°} \simeq \frac{\omega_0 C_P}{\omega_0 C_P + g_m} \simeq 1$. The oscillators may even lock in phase. Increasing g_m helps marginally but at the cost of extra voltage headroom or more capacitive parasitics.

Proposed Superharmonic Coupling Network
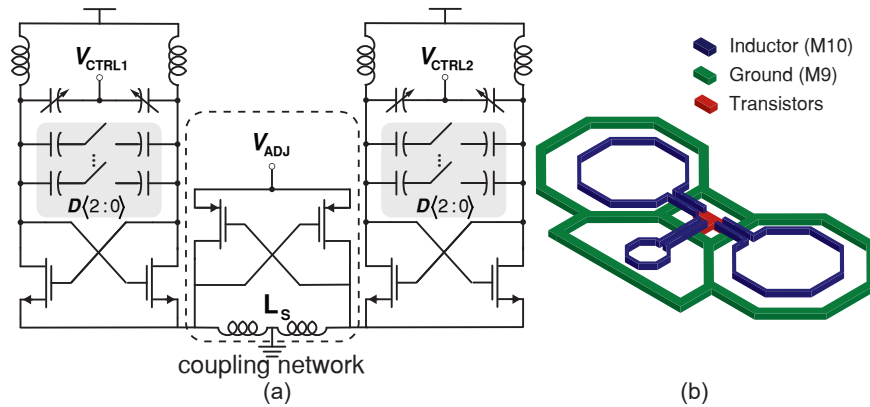
Figure 2.6: (a) Proposed QVCO schematic and (b) inductor Layout (not to scale) using M9/M10 (metal layer).

Fig. 2.6(a) shows the schematic of the implemented QVCO with proposed superharmonic coupling network. A third inductor L_S is employed to resonate out the parasitic tail capacitance at $2\omega_0$. It's worth mentioning that this additional inductor is very small compared with the tank inductors in the main oscillators (see Fig. 2.6(b)), because its operating frequency is doubled and the tail capacitance is usually high in the practical layout. After the capacitance is canceled, a PMOS cross-coupled pair is used to ensure quadrature locking in the same manner as depicted in Eq. (2.17), without consuming any oscillator voltage headroom. No high-pass biasing network ($R_B - C_C$ in Fig. 2.4) is required either.

It is well known that quadrature error occurs in the presence of oscillator mismatch. A nice feature of the proposed coupling network is that the quadrature accuracy under given tank mismatch can be adjusted with a control voltage V_{ADJ} without affecting the oscillator tanks. Assume due to mismatch the two oscillators locked in quadrature but with a small phase error equal to δ ($\delta \ll 1$). The voltage at the two coupled nodes (see Fig. 2.7(a)) can be

written as $S_+ = A_2 e^{-j(\delta+\pi/2)}$ and $S_- = A_2 e^{j(\delta+\pi/2)}$. Since the mismatch is small, reactance cancellation (L_S and C_P) still holds roughly. By applying KCL, the admittance at nodes $S_{+/-}$ is derived as following:

$$Y_{+/-}(\delta) = (-g_{m_p} + G_p)e^{\pm 2j\delta} + G_p \tag{2.18}$$

Note that $Y_+(\delta)$ and $Y_-(\delta)$ have same magnitude but opposite phases. Fig. 2.7(b) plots
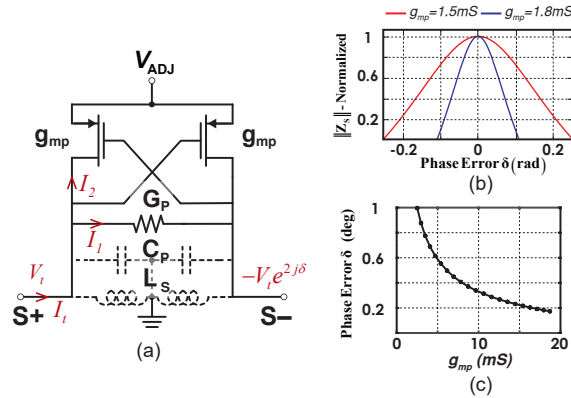
Figure 2.7: (a) $Z_{+/-}(\delta)$ nodal analysis under small mismatch, (b) calculated $\|Z(\delta)/Z(0)\|$ assuming $G_p = 1mS$ and $g_{m_p} = 1.5mS, 1.8mS$ respectively and (c) simulated quadrature error with 0.5% tank mismatch.

the normalized magnitude of tail impedance $\|Z(\delta)/Z(0)\|$ in the vicinity of $\delta = 0$ for two hypothetical g_{m_p} values. As shown in the plot, with a larger g_{m_p} value (higher V_{ADJ}), the tail impedance (and thereby the loop gain) sees a steeper downfall when deviating from perfect quadrature lock. This implies that as g_{m_p} increases, a higher level of mismatch is required to drag the two oscillators to a given phase error. In other words, the quadrature accuracy can be improved by increasing g_{m_p}. Fig. 2.7(c) plots the simulated QVCO phase error under 0.5% tank mismatch with different g_{m_p}. The error decreases monotonically as g_{m_p} increases. Therefore when the mismatch between the two oscillators do not meet the system requirements, one can increase g_{m_p} for better IQ accuracy with some power overhead.

QVCO Electrical Measurement Results

A 40GHz QVCO was designed and fabricated in 28nm bulk CMOS (no ultra-thick metal option). The die photo is shown in Fig. 2.8. The QVCO occupies 0.068mm² and consumes 8.4mW under 0.75V supply.

Tuning range and phase noise measurements are performed through on-wafer probing. As ground-signal-ground (GSG) pads are not available on chip, a Cascade infinity GS probe was landed in between the I/Q inductors to capture the near-field signal. The probe output is amplified with 65dB gain before feeding into the spectrum analyzer (Agilent N9030A) for
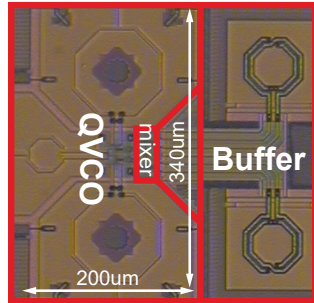
Figure 2.8: Chip micrograph of the proposed QVCO.
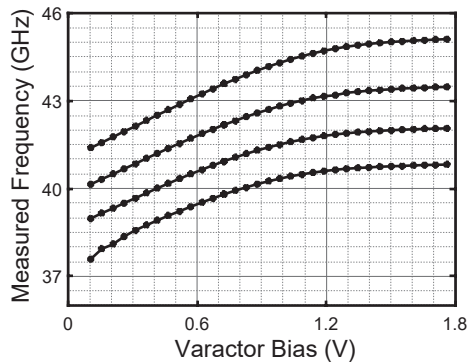
Figure 2.9: Measured frequency tuning curves.

phase noise measurement. The QVCO can be tuned from 37.5GHz to 45.1GHz, indicating a tuning range of 18.4%, as shown in Fig. 2.9. The QVCO exhibits a relatively constant phase noise level across the entire frequency tuning range, from -87.3dBc/Hz to -89.7dBc/Hz at 1MHz offset, corresponding to a FoM from -171dBc/Hz to -173dBc/Hz (see Fig. 2.10). The measured phase noise is not good and later sensitivity experiments reveal that the excessive phase noise comes from AM-PM conversion of noisy varactor control voltages which are generated using a DAC whose reference is merely a LDO digital supply (as the noise floor reduced by over $100\times$ after switching to a clean varactor control). However, the 65dB LO amplifier is no longer available which precludes retaking the phase noise measurements.

Quadrature accuracy is characterized through the DC product of I/Q self mixing (i.e., $\cos(\omega t - \delta/2)\sin(\omega t + \delta/2)|_{DC} \to \sin(\delta)$). To do this, a double-balanced voltage commutative passive mixer followed by a VGA (variable gain amplifier) is integrated on chip. Chopping is employed to remove DC offset and flicker noise. Fig. 2.11 shows the measured differential output $V_{OD,DC}$ as a function of V_{ADJ} and total QVCO power consumption. Quadrature error is back-calculated using the mixer phase-to-voltage conversion gain obtained from post-layout simulation, and plotted in the same figure. A phase error as low as 0.18° is achieved with V_{ADJ}=0.45V. Taking into account the extraction and model uncertainty, the actual phase
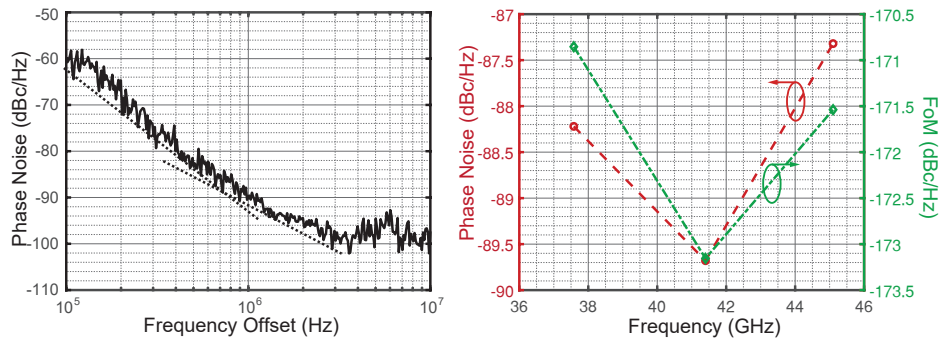
Figure 2.10: Measured (a) phase noise at 41GHz and (b) phase noise/FoM across tuning range.
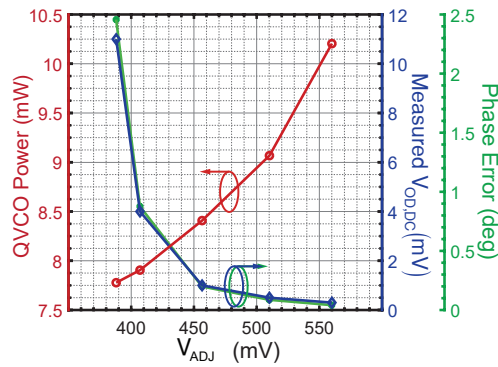
Figure 2.11: Quadrature accuracy and DC power measurement.
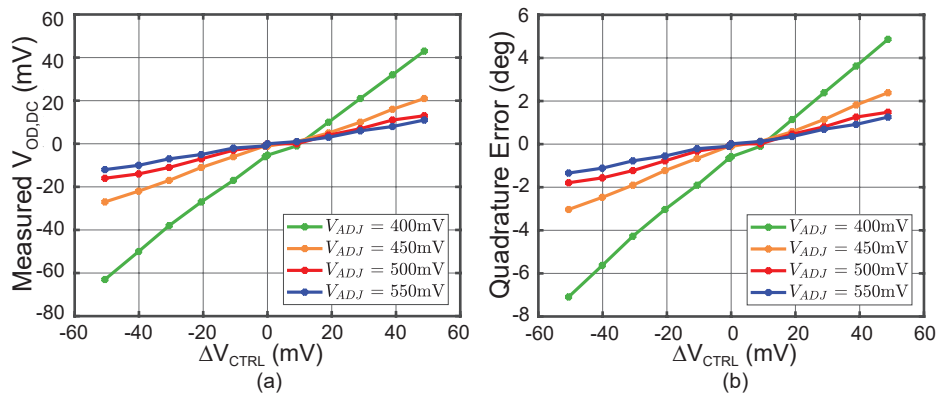
Figure 2.12: (a) Measured I/Q self-mixing differential DC output and (b) back-calculated phase error decrease as V_{ADJ} increases ($V_{CTRL,CM}$=1.2V).

error is believed to be less than 0.4°. To validate that the proposed coupling network can

improve phase accuracy using V_{ADJ} in the presence of mismatch, artificial offsets are created between the free-running frequencies of I/Q oscillators using individually-accessible varactor control voltages. Fig. 2.16(a) shows the measured differential output as a function of ΔV_{CTRL} under different V_{ADJ}. Fig. 2.16(b) plots the back-calculated phase error. It can be seen that as V_{ADJ} increases from 400mV to 450mV, 500mV and 550mV, respectively, a $2\times$, $3.3\times$ and $4\times$ improvement in quadrature accuracy is obtained.

Table 2.1: QVCO Performance Summary and Comparison

Reference	Coupling Method	CMOS Tech.	Freq. (GHz)	TR (%)	DC Power (mW)	Phase Error (deg)	PN @1MHz (dBc/Hz)	FoM* (dBc/Hz)	FoM$_T$** (dBc/Hz)	Adjustable Phase Accuracy
ISSCC'14[19]	Superharmonic	40 nm	58	16.2	30	2	-92.5	-173	-177	No
JSSC'14[20]	NMOS diode	65 nm	63	16.6	11.4	0.7	-94.2	-180	-184	No
TMTT'15[14]	Bidirectional diode	65 nm	26	15.4	11.8	0.36	-99	-176	-180	No
TMTT'16[15]	Transformer	65 nm	54	9.1	24	2	-95.5	-180	-179	No
This Work	Superharmonic	28 nm	41	18.4	8.4	0.18	-89.7	-173	-178	Yes

*FoM=PN-20$\log_{10}(\frac{f_0}{\Delta f})$+10$\log_{10}(\frac{P_{DC}}{1mW})$

**FoM$_T$=FoM-20$\log_{10}(\frac{TR[\%]}{10})$

Table 2.1 summarizes and compares this work with recent publications on mm-Wave QVCOs. A good tuning range and very low quadrature error is achieved with very low power consumption. A new mechanism of adjusting phase error against mismatch is provided.

2.3 Sensor Readout Scheme
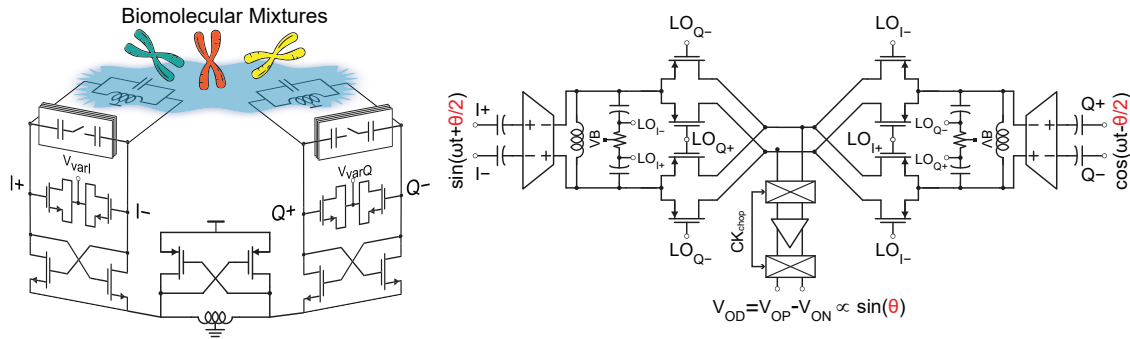
Figure 2.13: System architecture of the QVCO-based permittivity sensor: (a) superharmonic coupled QVCO and (b) phase detector (PD) including tuned buffer, mixer and chopped amplifier.

Fig. 2.13 shows the system architecture of the QVCO-based permittivity sensor implemented in this work. As discussed in Section 2.2, IQ phase difference is measured in a self-mixing fashion. A tuned buffer is inserted between the QVCO and the mixer to isolate

the LC tank from the IQ phase-dependent mixer load. A double balanced passive voltage driven mixer is used instead of Gilbert units to reduce flicker noise by biasing the PMOS switches at zero DC current. The mixer output is fed to a baseband amplifier whose offsets and flicker noise are suppressed by a chopping pair.

Since bio-reactions usually take minutes to hours long to create only small changes, special care is needed to suppress electronic noise to achieve good sensitivity and long-term stability. To address this challenge, existing solutions either use a replicated oscillator or rely on some specific external labels as a reference, which have limited effectiveness since a perfect replica does not exist when the sensing oscillator is loaded with samples and the required labels may not be suitable. On the contrary, this thesis proposes a novel tank-perturbation based readout scheme which doesn't require any label or replica reference at all. The sensing scheme is described first, followed with an analysis of its noise and sensitivity based upon the *Generalized Adler's Equation*[21]. Finally some electrical characterizations of the sensor sensitivity and long term stability is given.

Tank-Perturbation based Sensing Scheme
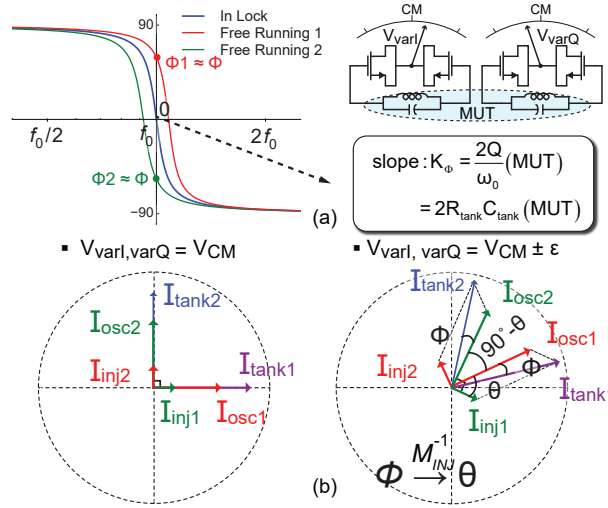
Figure 2.14: Illustration of tank-perturbation based sensing scheme using (a) tank impedance phase Bode plot and (b) phasor diagram.

As shown in Fig. 2.14(a), IQ inductors and sensing capacitors are equally exposed to the same bio-medium. With identical varactor bias, the two VCOs lock in quadrature at $\omega_0(\text{MUT})$ (MUT, material under test) and produce ideally zero differential output. To perform sensing, V_{varI} and V_{varQ} are offset in opposite directions by equal amounts ϵ to create a mismatch in IQ free-running frequencies. With a small tank perturbation, the two VCOs will lock back to $\omega_0(\text{MUT})$ but with a quadrature error θ, leading to a non-zero V_{OD}. According to the phasor diagram in Fig. 2.14(b), the quadrature error θ links to the tank

impedance phase angle ϕ with a factor inversely proportional to the relative injection strength M_{INJ}. Meanwhile, at a given frequency offset $\Delta\omega$, the phase angle ϕ depends on $\frac{Q}{\omega_0}(\mathrm{MUT})$, which reflects the dielectric properties of the surrounding bio-medium. In summary, the permittivity of the MUT can be extracted by exploiting the relationship between V_{OD} and $V_{\mathrm{varIQ,d}} \triangleq V_{\mathrm{varI}} - V_{\mathrm{varQ}}$

$$\theta = K_{\mathrm{VCO}}\left[\frac{2Q}{\omega_0}(\mathrm{MUT})\right]\left(1 + \frac{1}{M_{\mathrm{INJ}}}\right) \tag{2.19}$$

$$\frac{V_{\mathrm{OD}}}{V_{\mathrm{varIQ,d}}} = G_{\mathrm{mixer}}G_{\mathrm{baseband}} \times \theta \tag{2.20}$$

which gives

$$\frac{V_{\mathrm{OD}}}{V_{\mathrm{varIQ,d}}} = K_{\mathrm{VCO}}\left[\frac{2Q}{\omega_0}(\mathrm{MUT})\right]\left(1 + \frac{1}{M_{\mathrm{INJ}}}\right)G_{\mathrm{mixer}}G_{\mathrm{baseband}} \tag{2.21}$$

During an actual measurement, instead of measuring at single offset value, IQ varactor biases are swept differentially around a fixed common mode ($V_{\mathrm{varIQ,CM}}$) to produce a series of different V_{OD}. Linear regression is used to extract the slope of V_{OD} v.s. $V_{\mathrm{varIQ,d}}$ as the final readout. Sweeping and regression suppresses thermal noise to improve SNR. Moreover, slope extraction is equivalent to correlated double sampling (CDS), which removes the PD flicker noise. This is critical since the output signal V_{OD} is purely DC and it is challenging to implement RF chopping switches in between the QVCO and the tuned buffer without performance degradation.

Sensitivity Analysis

According to [22], there are in general two different phase noise generation mechanisms in a LC oscillator.

1. Current noise is injected into an ideal noise-free switching current, which modifies the periodic zero-crossing point and perturbs the oscillation phase. This applies to the resonator thermal noise, differential pair thermal noise and tail current noise (thermal and flicker, but only contributes AM not PM noise).

2. The effective resonator L or C is modulated by the noise source directly. For example, [22] points out that the differential pair flicker noise is up-converted to $1/f^3$ phase noise because the parasitic tail capacitance appears as part of the tank capacitance during a portion of the oscillation cycle but flicker noise changes that portion and thereby the effective tank capacitance.

The following analysis will mathematically show how the proposed sensing structure suppresses the above phase noise to achieve good sensitivity.

When two identical oscillators (natural frequency ω_0) are locked in quadrature through a phase shift ϕ, suppose the two differential output voltages are $A\exp(j\theta_1)$ and $A\exp(j\theta_2)$, where $\theta_1 = \omega_{\text{osc}}t$ and $\theta_2 = \omega_{\text{osc}}t + \pi/2$, the *General Adler's Equation* requires [21]

$$\begin{aligned}
\frac{d\theta_1}{dt} &= \omega_0 - \frac{\omega_0}{2Q}\frac{\sin(\theta_2 - \theta_1 - \phi)}{1 - M_{\text{INJ}}\cos(\theta_2 - \theta_1 - \phi)} \\
\frac{d\theta_2}{dt} &= \omega_0 - \frac{\omega_0}{2Q}\frac{\sin(\theta_1 - \theta_2 - \phi)}{1 - M_{\text{INJ}}\cos(\theta_1 - \theta_2 - \phi)}
\end{aligned} \tag{2.22}$$

In the case of the proposed superharmonic coupled QVCO, $\omega_{osc} = \omega_0$ and $\phi = -\pi/2$ due to in-phase injection locking. Suppose that θ_1 and θ_2 are perturbed as $\hat{\theta}_1 = \theta_1 + \theta_{1n}$ and $\hat{\theta}_2 = \theta_2 + \theta_{2n}$ due to the phase noise in each oscillator $\hat{\omega}_{01} = \omega_0 + \psi_{1n}$ and $\hat{\omega}_{02} = \omega_0 + \psi_{2n}$. Eq. (2.22) becomes

$$\begin{aligned}
\frac{d\hat{\theta}_1}{dt} &= \omega_0 + \frac{d\psi_{1n}}{dt} + \frac{\omega_0 + \frac{d\psi_{1n}}{dt}}{2Q}\frac{M_{\text{INJ}}\sin(\theta_{2n} - \theta_{1n})}{1 + M_{\text{INJ}}\cos(\theta_{2n} - \theta_{1n})} \\
\frac{d\hat{\theta}_2}{dt} &= \omega_0 + \frac{d\psi_{2n}}{dt} + \frac{\omega_0 + \frac{d\psi_{2n}}{dt}}{2Q}\frac{M_{\text{INJ}}\sin(\theta_{1n} - \theta_{2n})}{1 + M_{\text{INJ}}\cos(\theta_{1n} - \theta_{2n})}
\end{aligned} \tag{2.23}$$

The phase detector takes the difference between $\hat{\theta}_1$ and $\hat{\theta}_2$ so what matters is the 'differential' phase noise $\theta_n = \hat{\theta}_1 - \hat{\theta}_2$, which is

$$\frac{d\theta_n}{dt} = \frac{d\psi_{2n}}{dt} - \frac{d\psi_{1n}}{dt} + \frac{\omega_0}{2Q}\frac{M_{\text{INJ}}\theta_n}{1 + M_{\text{INJ}}} \tag{2.24}$$

Taking $s-$Transformation yields a high-pass transfer function,

$$\Theta_n(s) = \frac{s}{s + \omega_{\text{LR}}}(\Psi_{2n}(s) - \Psi_{1n}(s)) = H_{\text{HPF}}(s)(\Psi_{2n}(s) - \Psi_{1n}(s)) \tag{2.25}$$

where $\omega_{\text{LR}} = \frac{\omega_0}{Q}\frac{M_{\text{INJ}}}{1 + M_{\text{INJ}}}$ represents the injection locking range. Fig. 2.15(b) plots how $H_{\text{HPF}}(s)$ helps attenuate the close-in phase noise significantly. Note that the flicker phase noise corner frequency ω_{1/f^3} is pretty low in the proposed superharmonic QVCO since the inductor in the coupling network resonates out the tail capacitance, the major contribution to the flicker noise up-conversion.

Eq. (2.25) gives the phase noise spectrum at single point readout (i.e. a single set of IQ varactor control voltages). The correlated double sampling (CDS) performed during the process of sweeping and slope extraction adds a second high-pass filtering effect onto the noise spectrum[23],

$$H_{\text{CDS}}(\omega) = j2\sin(\omega T_{\text{CDS}}/2) \tag{2.26}$$

where T_{CDS} is the time interval between adjacent two samples. When $\omega T_{\text{CDS}} \ll 1$, Eq. (2.26) stimulates a differentiator,

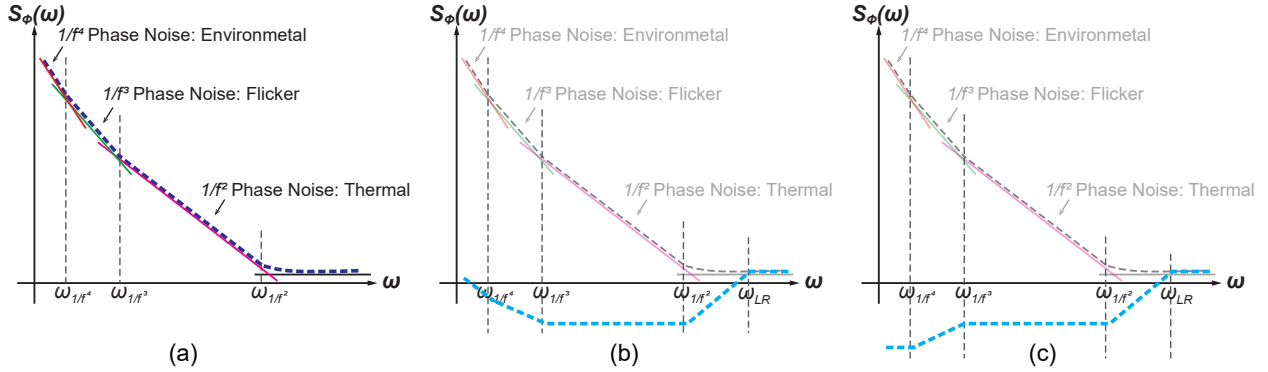$$|H_{\text{CDS}}(\omega)| \simeq \omega T_{\text{CDS}} \tag{2.27}$$

Figure 2.15: Illustration of phase noise spectrum with respect to the offset frequency ω of (a) QVCO single-oscillator output (dark blue) (b) QVCO dual-oscillator phase difference (light blue), and (c) after CDS (light blue).

which cuts flicker phase noise more, as shown in Fig. 2.15(c).

Therefore the total output phase noise can be written as

$$S_{\text{out,n}} = \left(S_{1\phi} + S_{2\phi}\right)|H_{\text{HPF}}(j\omega)H_{\text{CDS}}(\omega)|^2 = \left(S_{1\phi} + S_{2\phi}\right)\left(\frac{\omega^4 T_{\text{CDS}}^2}{\omega^2 + \omega_{\text{LR}}^2}\right) \qquad (2.28)$$

The minimal detectable frequency resolution normalized by ω_0 is then

$$\left(\frac{\Delta\omega}{\omega_0}\right)^2\Big|_{\text{RMS,n}} = \frac{\int_{-\infty}^{+\infty} S_{\text{out,n}} d\omega}{\left(K_{\text{VCO}}(2Q)(1 + M_{\text{INJ}}^{-1})\right)^2} \qquad (2.29)$$

The two-fold high-pass filtering effect produces 40dB/dec close-in phase noise reduction, which is sufficient even for environment-related $1/f^4$ phase noise suppression. Note that the signal of interest is the tank property in Eq. (2.19), so the multiplicative noise from injection current has to be attenuated by averaging.

The proposed reactance sensing structure can be reconfigured into reference-sensing modality as well. One of the two quadrature coupled oscillators serves as reference (with no samples loaded) and the other is loaded with samples. Single-point direct phase readout scheme (no CDS) will then be performed. Compared with unidirectional-locked-oscillator (UILO) based sensor, the phase shift is halved due to mutual injection but the output phase noise is more than half if the phase noise from external excitation source and injection devices can be perfectly canceled in the UILO case, which leads to a degradation of SNR. However, the QVCO-based scheme consumes less than half of the UILO power, so it overall offers a better performance.

Sensor Electrical Characterization

The sensor sensitivity is limited by the frequency noise floor, which is usually represented by the ratio of the oscillator frequency variance (i.e. frequency noise) over the oscillator center frequency. In the proposed phase slope readout scheme, the frequency variance is characterized by input-referring the output slope variance $\sigma(K_{\text{sig}})(= \sigma(\partial V_{\text{OD}}/\partial V_{\text{varIQ,d}}))$ with assistance of an intermediate variable: the QVCO varactor control common-mode $V_{\text{varIQ,CM}}$, since

$$\frac{\partial f_{\text{osc}}}{\partial K_{\text{sig}}} = \frac{\partial f_{\text{osc}}}{\partial V_{\text{varIQ,CM}}} \frac{\partial V_{\text{varIQ,CM}}}{\partial K_{\text{sig}}} \tag{2.30}$$

First of all, the tuning range of the QVCO, K_{VCO} ($= \partial f_{osc}/\partial V_{\text{varIQ,CM}}$) and sensor transducer gain $A_{\text{T}}(= \partial K_{\text{sig}}/\partial V_{\text{varIQ,CM}})$ are measured separately. Next, the rms noise of K_{sig} at a fixed $V_{\text{varIQ,CM}}$ is measured by taking 300 samples continuously. Therefore the frequency sensitivity is derived as:

$$\frac{\sigma f}{f_0} = \frac{\sigma(K_{\text{sig}}) \times K_{\text{VCO}}/A_{\text{T}}}{f_0} \tag{2.31}$$

As shown in Fig. 2.16, at $V_{\text{varIQ,CM}} = 1.3$V, the frequency sensitivity is 3.1ppm ($K_{\text{VCO}} = 0.72$G/V, $f_0 = 41.88$GHz). 1.32ppm sensitivity can be obtained at $V_{\text{varIQ,CM}} = 1.5$V by imposing some bias stress onto the varactors.
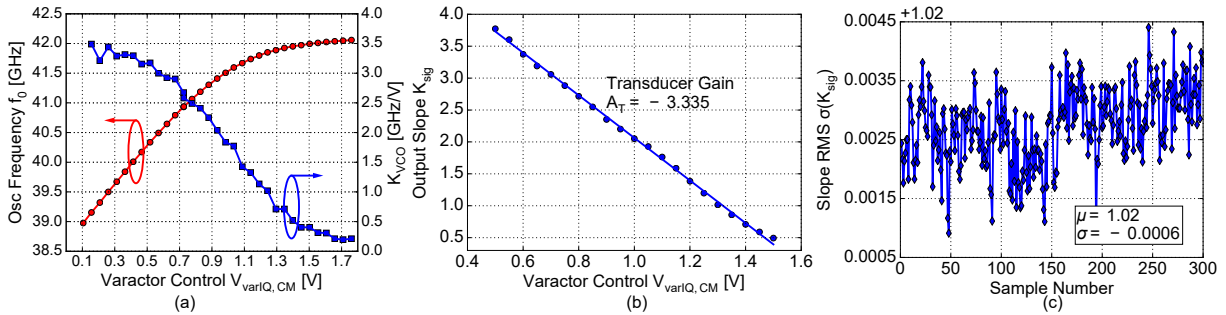
Figure 2.16: Measured (a) QVCO tuning range and KVCO, (b) sensor transfer curve, and (c) output slope K_{sig} variations.

To characterize long-term stability, a continuous 8-hour long experiment was preformed on the laboratory bench, during which period 10 samples of K_{sig} were measured every 5 minutes. Thanks to the noise attenuation capability of the proposed sensing scheme, an excellent 5.4ppm stability is achieved at $V_{\text{varIQ,CM}} = 1.3$V with no replica reference or any specific labels, as shown in Fig. 2.17.
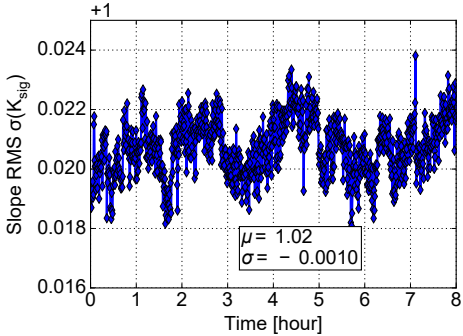
Figure 2.17: Long-term stability test: an 8-hour measurement of output slope K_{sig}.

Chapter 3

SPAD Optical Sensor

Optical sensors are another commonly reported class of biosensors since the light signals produced by biological reactions offer good sensitivity and specificity. Therefore, integrating optical sensors on the same CMOS chip along with the mm-wave permittivity sensors are of great advantages. Typical optical detection is based on the measurement of luminescent, fluorescent, colorimetric or other optical signals generated during the interactions of biological samples. Compared with conventional reverse-biased PN junction diodes, single photon avalanche diodes (SPADs) are preferred since they

- offer single-photon level sensitivity

- detect photon arrival time and can be used as fluorescence lifetime measurements without any optical filters

- have superior electronic noise immunity due to its digital operating nature

The increased doping concentration in sub-100nm CMOS proceesses reduces the junction width by decreasing the breakdown voltage (thus smaller active sensing volume) but increases band-to-band tunneling (thus higher noise). However, scaling down to sub-100nm process nodes brings about the benefits of fast logic speeds (thus better timing), higher integration density (thus higher fill factor) and reduced overall cost. Therefore lots of research efforts have been devoted in developing SPADs in these technologies.

This chapter begins with a brief description of SPAD operation mechanism and important performance parameters in Section 3.1. Section 3.2 presents the device and circuit implementation details of SPADs for the first time in 28nm bulk CMOS process. Electrical characterization results will be given in Section 3.3.

3.1 SPAD Figures of Merits

The basic structure of a SPAD is a reverse-based pn junction. Unlike an ordinary photodiode, the SPAD is biased with a large negative potential over the junction breakdown voltage, which produces a large electrical field across the depletion region (called multiplication region). Carries flowing through this region get accelerated and collide with the silicon lattice atoms to produce more carries. The new carriers experience the same process to generate even more free carriers. This process is called impact ionization, as shown in Fig. 3.1(a). The large current generated can be modeled with a multiplication factor M [24]

$$J = M J_{s0}$$
$$M = \frac{1}{1 - (\frac{V_R}{V_{BR}})^n} \tag{3.1}$$

where J_{s0} is the reverse saturation current, V_R is the applied voltage and V_{BR} is the breakdown voltage. n is a constant value between 3 to 5. The breakdown voltage depends on the diode geometry, semiconductor type and doping concentration. When V_R approaches V_{BR}, M goes to infinity and even one single electron in the multiplication region can trigger a large current. Therefore a SPAD is usually biased at $V_R > V_{BR}$.
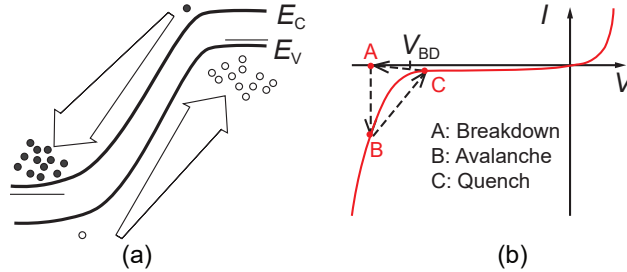
Figure 3.1: (a)Energy band diagram showing avalanche breakdown and (b) IV curve of SPAD operation in continuous detection mode.

Because the avalanche current is self-sustainable, an external quencher is required so that the SPAD can detect incoming photon continuously. A quencher will move the SPAD out of the avalanche region by decreasing the reverse bias voltage at the onset of an avalanche breakdown. Once the current in the depletion region vanishes, the quencher deactivates itself and biases the SPAD back into the single-electron/photon sensitive region, awaiting the next event (see Fig. 3.1(b)).

Important performance parameters of a SPAD include (1) photon detection efficiency (PDE), (2) dark count rate (DCR) and (3) timing uncertainty (jitter).

Photon Detection Efficiency

Photon detection efficiency (PDE) describes the optical sensitivity of the SPAD, which is defined as the probability of an avalanche event triggered by an incoming photon at a given wavelength. It is the product of the probabilities for two consecutive processes: photon absorption and electron multiplication. Photon absorption is approximated by the *Beer-Lambert Law*,

$$I(x) = I_0 e^{-\alpha x} \tag{3.2}$$

where I_0 is the intensity of the incident light, x is the depth along the photon trace, and α is the absorption coefficient. α depends on the photon wavelength and semiconductor type [24]. The photon penetration depth $d(\lambda) = 1/\alpha$ describes the average depth a photon reaches before getting absorbed and starting the second process - electron multiplication. The overlap of this penetration depth and the depletion region determines the overall sensitivity of a given SPAD at certain wavelength.

Doping and bias can be engineered to tune the wavelength sensitivity. In the case of designing SPADs in a commercial CMOS process, one can select the combination of device layers for p-side and n-side of SPADs or change the excessive bias voltage $V_{\text{EX}} = V_{\text{B}} - V_{\text{BR}}$ to optimize the PDE at the desired wavelength. Increasing V_{EX} usually helps to improve PDE but at the cost of higher noise level (DCR), so there is usually an optimal V_{EX} for best SNR.

Dark Count Rate

Dark count rate (DCR) describes the noise property of the SPAD, which is characterized by the frequency of avalanche events in the absence of light. Dark events are triggered by thermally generated carriers and band-to-band tunneling. Most thermal carrier generation is assisted by recombination-generation centers which are created by the local impurities and lattice defects. Since these recombination-generation centers are located within the band gap, they can increase the probability of carrier generation exponentially. Moreover, these trapping centers can be filled with carriers during an avalanche process or by high-intensity incoming light. The subsequent release of a carrier during the next detection cycle will cause the dark noise to propagate, known as an 'after pulse'. Most advanced CMOS technology nodes involve complicated band engineering to increase carrier mobility, which unavoidably introduces lots of defects and worsens the SPAD noise performance. On the other hand, band-to-band tunneling is only an issue when the doping concentration is very high, so high-doping layers such as diffusion layers for drain/source should be avoided when making a SPAD.

Timing Uncertainty

Since a SPAD can detect the arrival time of an incident photon, its timing accuracy is also a very important performance parameter. Jitter in SPADs is determined by the variance of

the difference between the avalanche event time and the photon arrival time and is usually reported as the full width half maximum (FWHM) of the detected photon arrival time distribution under an external ultrafast pulsed laser.

In a SPAD, the statistical timing curve typically exhibits two components: (1) a fast narrow distribution around the actual photon arrival time followed by (2) a slow tail[25]. The fast narrow distribution corresponds to the avalanche process build-up time, which is a function of the excessive bias voltage V_{EX} and the junction volume (area and depth). High V_{EX} increases the multiplication factor and reduces FWHM, whereas large device sizing increases the lateral avalanche propagation time as well as parasitic capacitance. Moreover, the fluctuation of the actual photon absorption location in the depletion region adds more jitter. The slow tail, on the other hand, is mostly caused by photons that are absorbed outside the depletion region. Primary carriers generated outside the multiplication region need to go through a slow diffusion process to trigger an event, which generates a slow tail in the SPAD impulse response. Moreover, the surrounding readout circuits also contribute extra Gaussian electronic jitter that is eventually convolved with the SPAD impulse response.

3.2 Device and Circuit Implementation

SPADs are implemented in 28nm bulk CMOS for the first time, which is of great importance since it enables simultaneous ultra-sensitive optical and electrical sensing of localized biological environments. This Section covers the device design considerations of SPADs in 28nm CMOS as well as the readout circuits.

Device Layer

Generally speaking, there are two types of avalanche diodes that are fabricated in dedicated silicon technologies as shown in Fig. 3.2 [26]. The lateral structure has a thicker active region and thus has a better PDE. The vertical structure, on the other hand, has moderate PDE but a much better timing performance. However, many extra design constraints are introduced when integrating SPADs into standard CMOS technologies. For example, one single P-doped silicon is used as a common substrate in bulk CMOS technologies and this substrate has to be tied to $0V$. These constraints make it almost impossible to implement the lateral thick SPADs in standard CMOS. Fortunately, most advanced CMOS process enables twin-well and retrograde deep nwell to enhance noise isolation, which can also be leveraged to implement the vertical SPAD structures, as shown in Fig. 3.3 [27].

However, electric field uniformity can be a problem in such planar structures. First of all, bias voltage is applied from the top side, resulting in premature edge breakdown (PED), where the horizontal electric field E_x and E_y at the edge is the strongest. However, probabilities for a photon hitting the edge is negligible. Additionally, curvature of a square SPAD causes corner electric field intensity to be much higher, which is not favored either. The most
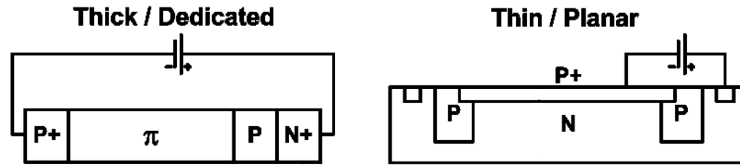
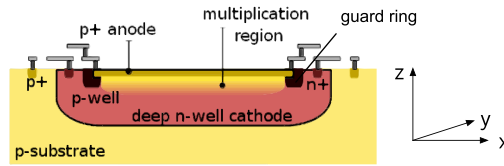Figure 3.2: Two types of silicon SPAD fabricated in dedicated technologies

Figure 3.3: An example of SPAD implemented in standard CMOS

effective solution to PED is to add a lightly doped region as guard ring to reduce the edge electric field. Circular structures are implemented instead of square structures to address the curvature issue. Moreover, advanced deep sub-μm CMOS technologies are featured with highly doped diffusion regions, SiGe-strain and reduced annealing, which introduce more defects and thereby only well layers (p-doped well (PW), n-doped well (NW) and deep-n-doped well (DNW)) and p-substrate (Psub) are considered in this design. Fig. 3.4 shows the SPAD device layer diagram and the device simulation setup in *Lumerical*. Doping concentrations are defined with *Lumerical* diffusion doping objects (Gaussian) and the doping level/profile are estimated based on previous works [28, 29]. Table 3.1 summarizes the peak doping value of different wells.
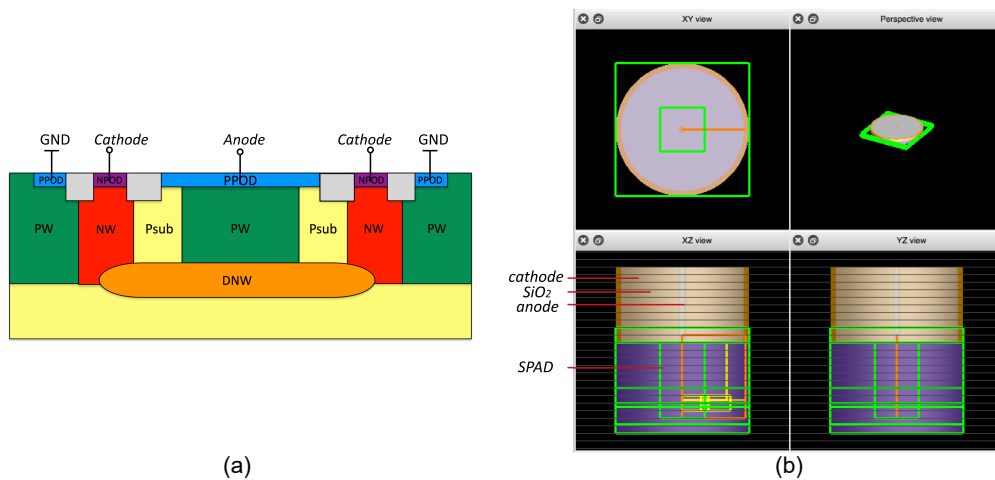

Figure 3.4: (a) SPAD device layer structure and (b) simulation setup in *Lumerical* DEVICE.

Electric field distribution in the following two cases are simulated:

Table 3.1: SPAD Doping Profiles

Well	Peak Doping (cm^{-3})	Profile	Depth (μm)
Psub	1×10^{15}	Uniform	N.A.
PW/NW	3×10^{18}	Gaussian	0.75
DNW	3×10^{18}	Retrograde	0.4

- Circular active region with P-substrate guard-ring,

- Circular active region without guard-ring,

Note that the simulation was conducted within a 3D geometry to capture a full picture of $\vec{E}$ field. Since the circular structure has a radial symmetry, only a slice of rectangle along radius was simulated to save time. Moreover, the boundary condition were set to be $15V$ across all the simulations, and the bias point has no essential influence on the conclusion drawn here. On the other hand, it shall be shown that a proper designed guard ring is crucial to avoid premature edge breakdown.

Circular Active Region with P-substrate Guard Ring

The dashed orange rectangle in Fig. 3.4(b) represents the cross section of the simulation region. The third dimension of the simulation region is very narrow since the structure is symmetric.

Fig. 3.5(a) shows the doping profile of the SPAD structure, where the dark blue, light blue, green and yellow region represent PW, Psub guard ring, DNW and NW, respectively. Due to the lower-doped Psub guard ring, sidewall edge $\vec{E}$ field is greatly reduced, as shown in Fig. 3.5(b) and (c), where (c) is 2D $\vec{E}$ field plot on XY plane at the depletion region. The effectiveness of the guard ring can also be validated from the 1D $\|E_X\|,\|E_Y\|,\|E_Z\|$ plot from Fig. 3.5(d). The strongest electric field is along the z direction (vertical), which is consistent with the junction orientation having the largest detection area. Meanwhile, the unwanted edge electric field $\vec{E_X}$ caused by such lateral structure is kept small.

Multiple simulations assuming different doping concentrations/profiles and other types of guard rings (e.g. N-sub guard ring, low-Vth PW guard ring) were performed. They all produced similar results, indicating the universal effectiveness of guard ring.

Circular Active Region without Guard Ring

To simulate without any guard ring, NW is extended to be in touched with PW. Fig. 3.6 shows the simulation results. It is clear from the dark red spot in Fig. 3.6(b) that the strongest electric field moves to the junction sidewall, causing premature edge breakdown and reducing detection efficiency. 1D plot in Fig. 3.6(c) and (d) split the field into $\vec{E_X}$, $\vec{E_Y}$ and $\vec{E_Z}$ at the sidewall ($z = -0.6\mu m$, see 3.6(b)) and at the bottom (z = -0.8μm),
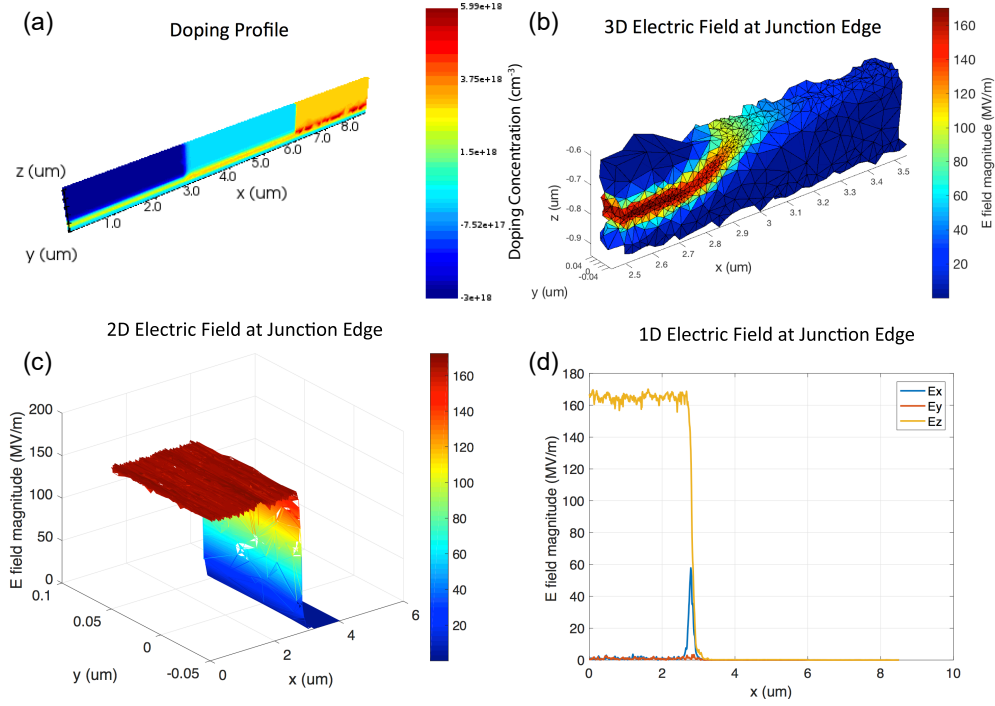
Figure 3.5: Circular active region with P-Sub guard ring

respectively.   Sidewall $\vec{E_X}$ is the highest, which supports the argument that E-field non-uniformity is caused by applying bias voltage from topside in such a planar structure.

Pixel Circuit

Fig. 3.7 shows the pixel schematic of the SPAD-based optical sensor and its device layer cross section. Each SPAD has $6 \times 6\mu m^2$ circular active area formed by Pwell-DeepNwell, surrounded by a native P-substrate to avoid edge breakdown and tunneling. SPAD anodes are biased at -14.5V to operate in Geiger mode. For continuous single photon detection, an external CLK is fed in to generate nonoverlapping ϕ_1 and ϕ_2 to control the NMOS active quencher and PMOS pre-charger respectively. This CLK can also be synchronized to a pulsed laser to perform FLT measurement. As shown in the timing diagram, after ϕ_1 turns off the M_N, the SPAD is activated by ϕ_2 through M_P. Upon a photon or dark event, avalanche current begins to discharge the SPAD cathode VK. The falling edge of VK triggers the DFF to turn off M_P and turn on the quencher M_N. A positive feedback is thereby formed to sharpen the falling edge and to keep the SPAD off to avoid afterpulsing. If no event occurs within a preset detection window, ϕ_1 will deactivate SPAD and set DFF high asynchronously until the next cycle. Both TRIG and VK can be configured as digital outputs for photon counting and FLT measurement.
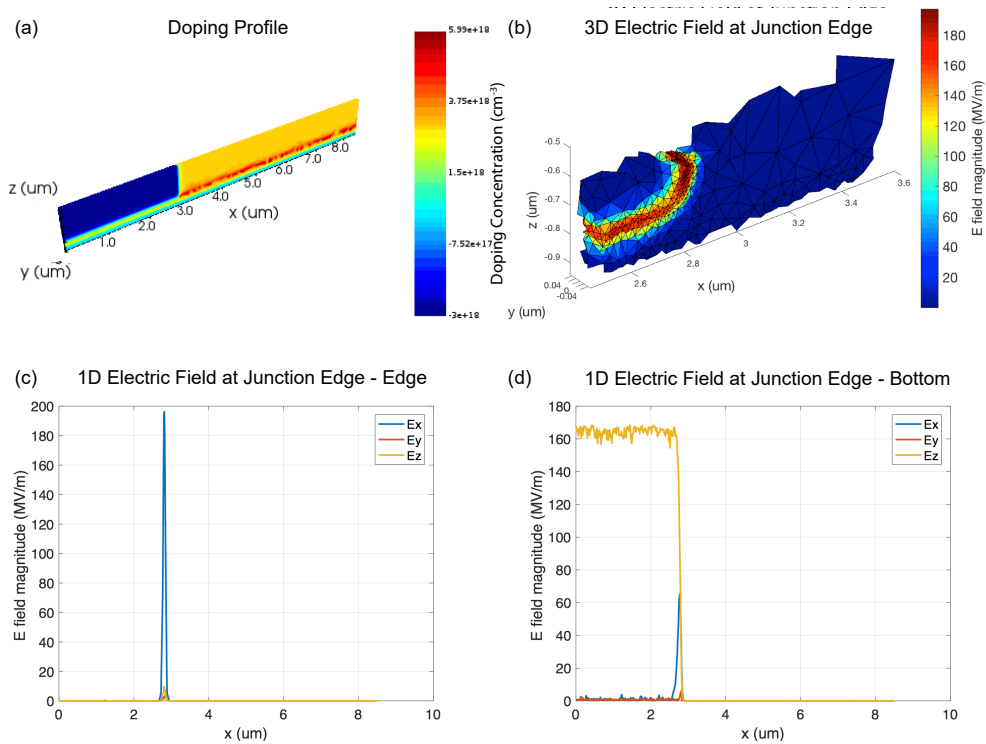
Figure 3.6: Circular active region without guard ring

3.3 SPAD Electrical Characterization

The measured avalanche breakdown voltage at room temperature is 15.3V (when V_{ANODE} =-13.5V, since the cathode is set to 1.8V through M_{P}), as shown in Fig. 3.8. Both the breakdown voltage and dark current are increased when the temperature is increased from $25°C$ to $40°C$, which reveals that the implemented P/N junction is under avalanche breakdown rather than band-to-band tunneling breakdown, as the breakdown voltage of the latter exhibits a negative temperature coefficients.

The uniformity of the electric field in the junction depletion region is verified using light-emission test[30]. This technique uses the fact that impact ionization can also generate photons (most dark red light) so that one can visualize the location of avalanche events over a given integration time. Fig. 3.9 shows light emitted from a solid circle rather than a annular ring, which indicates a uniform electric field distribution.

The dark count rate (DCR) is measured at room temperature with different excessive bias voltages V_{EX} set through V_{ANODE}. An external 1MHz CLK is used to gate the SPADs with 70% on-cycle and an accumulated 10-sec measurement is performed to characterize DCR. The reported count rate in Fig. 3.10 equals the measured count rate divided by the 70% on-cycle to calibrate out the 30% dead time. At V_{EX} =1V, each SPAD achieves a DCR
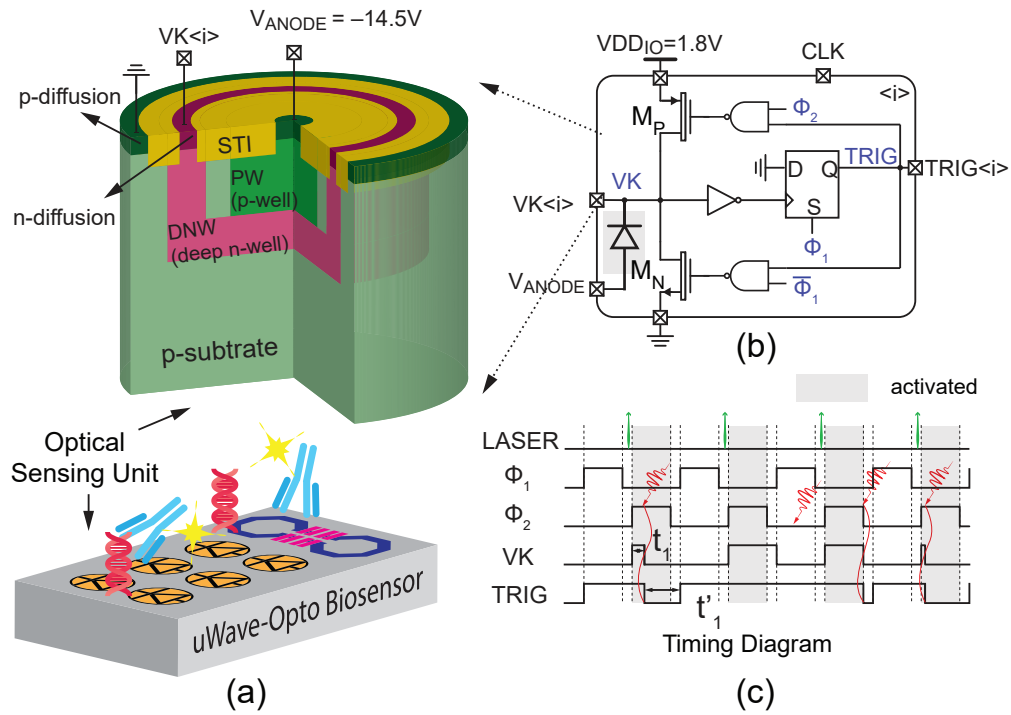
Figure 3.7: Pixel schematic of SPAD-based optical sensing unit: (a) device layer, (b) readout circuits and (c) operational timing diagram.

Figure 3.8: Single device I-V measurement at $25°C$ and $40°C$.

of as low as 500/sec.

The photon count rate (PCR) is measured in a similar fashion with three laser sources at different wavelengths (blue, green and red, optical power attenuated heavily by an ND filter before applying to SPADs) to characterize photon detection efficiency (PDE). The

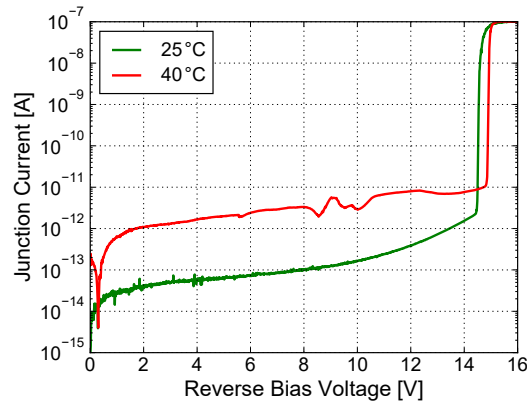Figure 3.9: Single device light emission test. The uniform circular bright region indicates a uniform electric field distribution and thereby a working device.
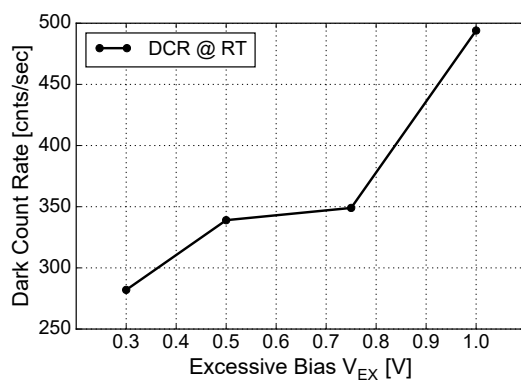

Figure 3.10: SPAD dark count rate (DCR) at different excessive bias voltage V_{EX}.

measurement results are plotted in Fig. 3.11. At V_{EX} =1V and 520nm incident green light, each SPAD achieves a PCR of 500/sec (3 order magnitude higher than DCR at the same V_{EX}) and PDE of 11.5%.

The impulse response (timing jitter) of the SPAD at V_{EX} =1V is measured using a 1044nm 300fs laser (frequency doubled to 522nm, with 1MHz repetition rate). The histogram in Fig. 3.12 shows a FWHM value of 300ps, a combined timing uncertainty of the SPAD device, readout circuits and external TDC as well as laser synchronization tools.

Table 3.2 summaries SPAD performance and compares with the state of art[31–34]. It is demonstrated that SPADs are implemented in 28nm bulk CMOS process for the first time with good DCR, PDE and jitter performance.
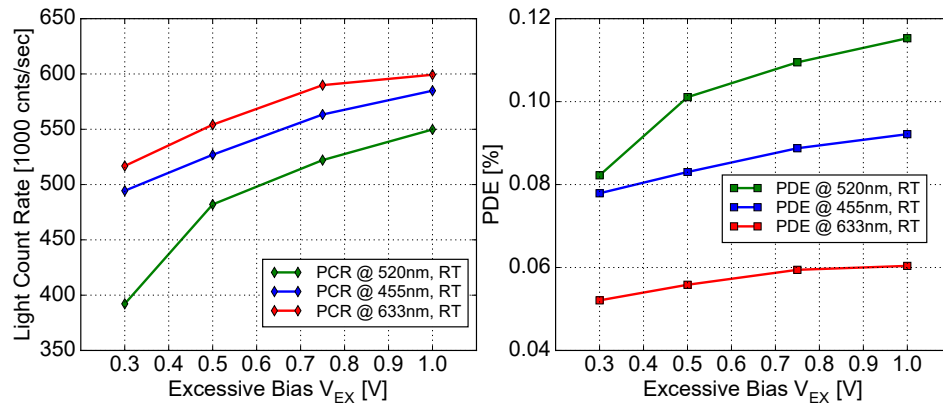
Figure 3.11: SPAD photon detection efficiency (PDE) at different excessive bias voltage V_{EX} and three different wavelengths.
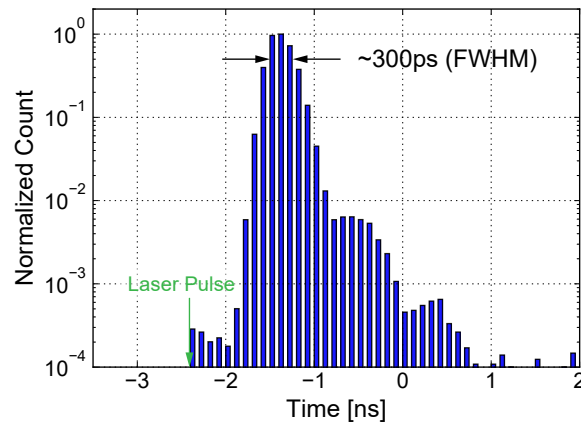
Figure 3.12: SPAD impulse temporal response at $V_{EX} = 1V$.

Table 3.2: SPAD Implemented in sub-100nm CMOS Processes

	Karami IISW'11	Charbon IEDM'13	Pellegrini IEDM'17	Albuquerque ESSDERC'18	**This work**
Technology	90nm CMOS†	65nm CMOS†	40nm CMOS†	28nm FDSOI	**28nm CMOS†**
Device Layer	Ndiff - Psub	Ndiff - Pwell	Pwell - DNwell	Pwell - DNwell	**Pwell - DNwell**
Diameter	8 µm	8 µm	N.A.	25 µm	**6 µm**
Breakdown Voltage	10.4 V	9.1 V	15.5 V	9.6 V	**15.3 V**
DCR (@ RT)	8100 cps (VEX = 0.13V)	500K cps (VEX = 0.25V)	50 cps (VEX = 1V)	~28000 cps (VEX = 0.3V)	**500 cps (VEX = 1V)**
PDE (@ RT)	12% (VEX = 0.15V)	5.5% (VEX = 0.25V)	30% (VEX = 1V)	N.A.	**11.5% (VEX = 1V)**
Timing Jitter	435 ps	235 ps	170 ps	N.A.	**~ 300 ps**

†CMOS refers to bulk CMOS

Chapter 4

Measurement Results

A sensor is fabricated in TSMC 28nm bulk CMOS process. It occupies $1.2{\times}1.0\text{mm}^2$ area in total. The prototype contains one QVCO-permittivity sensing site and 8 SPAD-optical sensing sites. Fig. 4.1 shows the chip photo as well as the layout view of a SPAD pixel. A bio-reaction cavity is created by aligning a slab of drilled Polydimethylsiloxane (PDMS) to the sensor chip on the PCB. Adhesion bonding and mechanical pressure are used to prevent ionic medium leakage which can cause PCB failure. Fig. 4.2 shows the packaging.
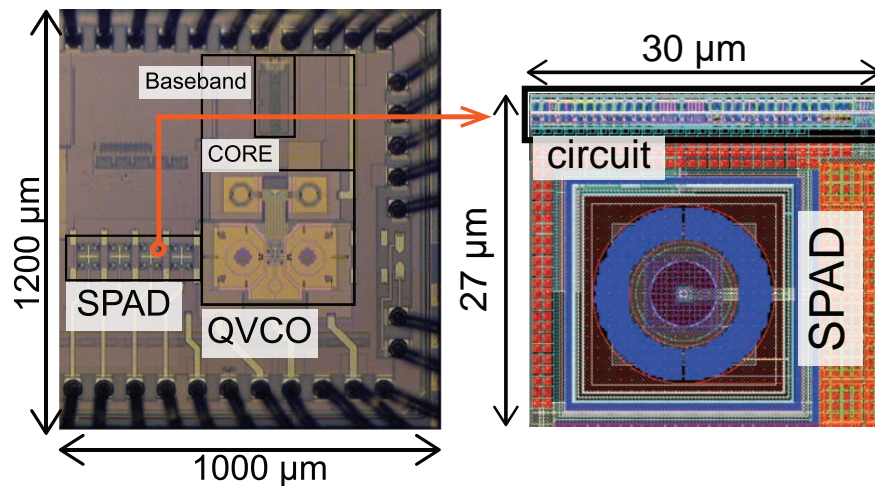

Figure 4.1: Chip micrograph.

The QVCO-based permittivity sensor and the SPAD-based optical sensor are tested with some sample liquids separately to characterize their performance. Then an enzyme denaturation experiment is performed with both sensors enabled to show that multi-parametric sensing provides a better profiling of complex biomolecular processes.
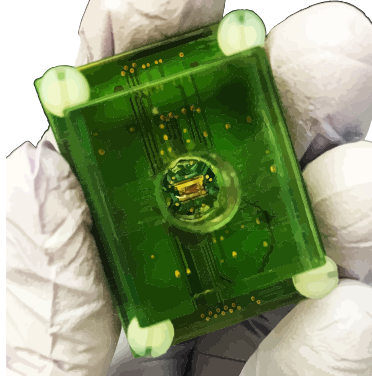
Figure 4.2: Biochemical reaction cavity packaging photo.

4.1 QVCO-based Permittivity Measurements

This Section shows the measurement results of various sample liquids using the proposed tank-perturbation based sensing method. As depicted in the sweep plan (Fig. 4.3), instead of measuring at one offset value, IQ varactor biases are swept differentially around a fixed common mode to produce a series of different $V_{\rm OD}$. Linear regression is used to extract the slope of VOD versus $V_{\rm varIQ}$ as the final readout. Sample liquids can be differentiated with single point sensing, where single cap-DAC code and varactor IQ CM are used during sweep. As shown in Fig. 4.4, four different liquids (DI water, 1-octanal, ethylene glycol and IPA) were measured at 44GHz (measured in Air) frequency band and they demonstrate different slope characteristics.
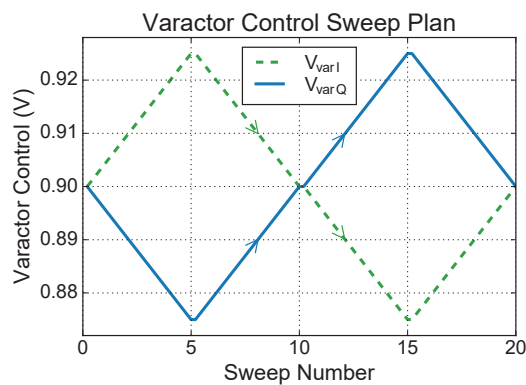

Figure 4.3: QVCO measurement varactor control sweep plan illustration.

Moreover, liquid dispersion properties can be characterized by varying cap-DAC codes to allow further differentiation. For instance, DI water demonstrates different slope values
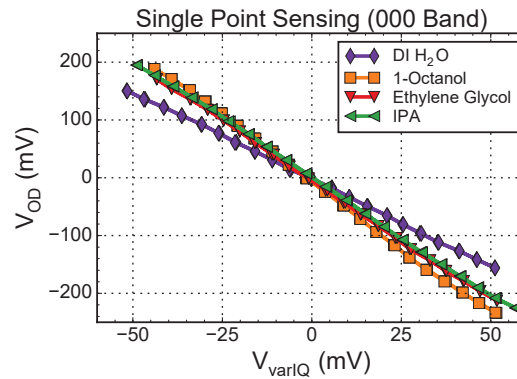
Figure 4.4: QVCO measurement of different liquids at single frequency point.

when the cap-DAC code changes (see Fig. 4.5(a)). In addition, IPA and ethylene glycol have almost the same slope in the single point sensing but can be distinguished with dispersion sensing (see Fig. 4.5(b)). Note that measurements taken in air are used as reference to separate material dispersion from electronic dispersion, the latter of which results from cap-DAC switching in/out.

Figure 4.5: QVCO measurement varactor control sweep plan illustration.

4.2   SPAD-based Optical Measurements

This Section shows the experimental results when the SPADs are configured to measure fluorescent lifetimes. Specifically, the lifetime of a fluorescent biomolecule Rhodamine6G (Rh6G) at different iodide concentrations was measured. Rh6G fluorescence undergoes

a first-order diffusion controlled quenching by iodide[35] and is often exploited to generate convenient mono-exponential decay standards. It suffices for accurately calibrating a lifetime-measurement tool a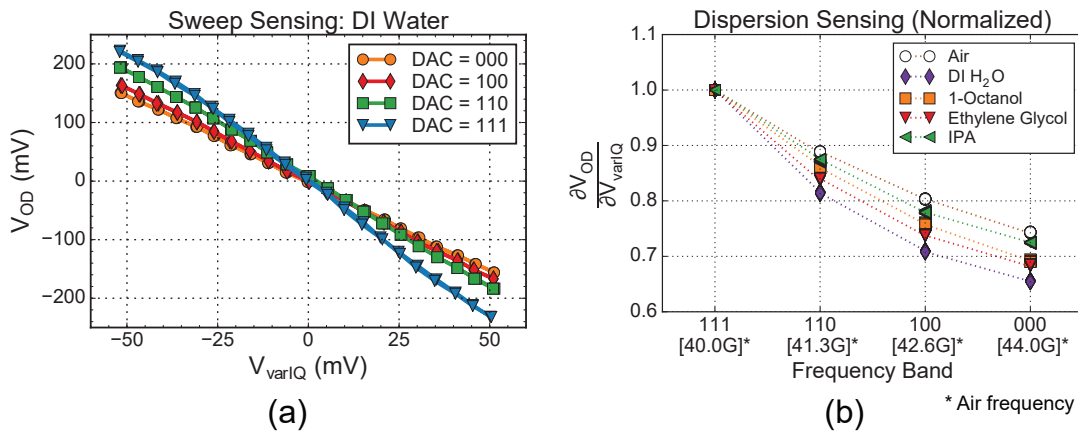nd is therefore used to characterize the SPAD performance. The relationship between the observed lifetime τ_f and the quencher concentration $[Q]$ is given by

$$\frac{1}{\tau_f} = k_q[Q] + \frac{1}{\tau_f^0} \tag{4.1}$$

where k_q is the bimolecular rate constant for quenching and τ_f^0 is the fluorescence lifetime in the absence of the quencher. The typical fluorescence lifetime range due to iodide quenching reaction is between 0.5-4.1ns.
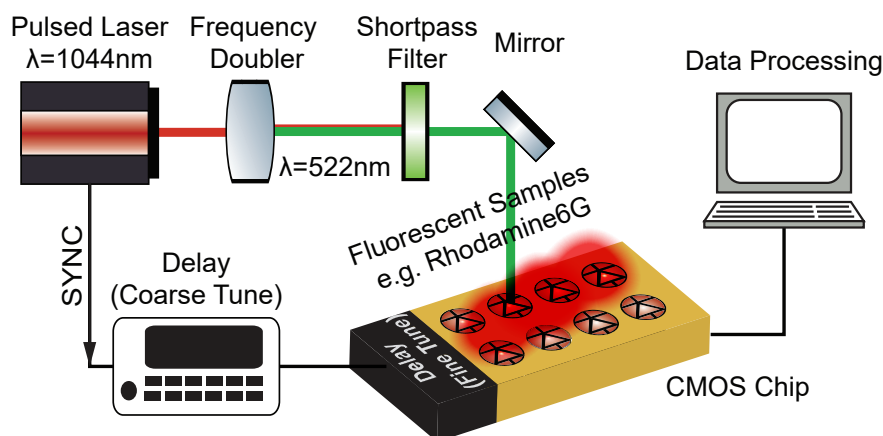

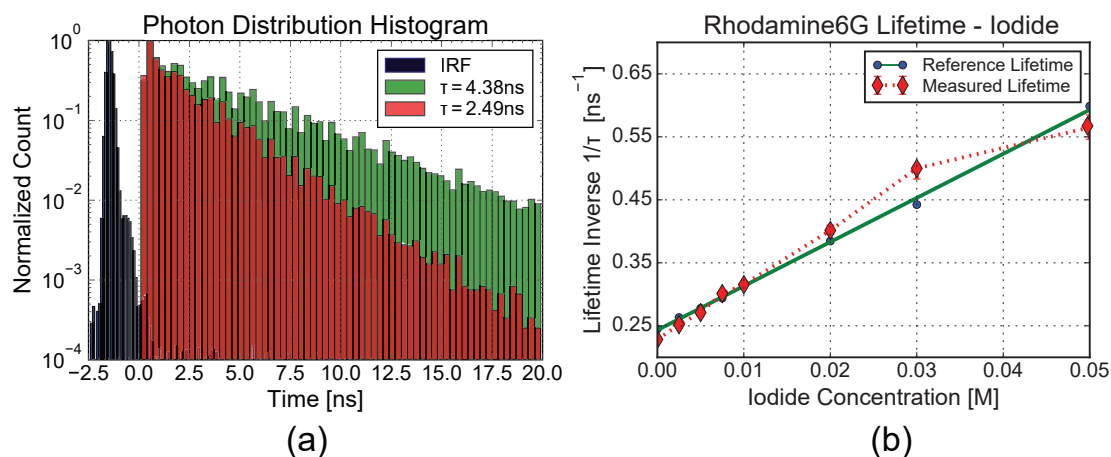Figure 4.6: SPAD fluorescence lifetime measurement setup.

Figure 4.7: Lifetime measurement of iodide quenched Rhodamine6G.

Fig. 4.6 shows the lifetime measurement setup. A 1044nm 300fs laser (frequency doubled to 522nm) with 1MHz repetition rate serves as the excitation source. Rh6G emission is detected by SPADs and the digital outputs are captured for lifetime extraction. When synchronizing the SPADs to the laser, an extra 1.5ns gating window obviates the need for filters by attenuating the excitation light 5000x (see the instrumental response (IRF) histogram in Fig. 4.7(a)). The measured Rh6G lifetimes shown in Fig. 4.7 agree with the reference values [35] very well.

4.3 Dual-Modality Measurements

Fig. 4.8 shows a time-lapse study on the thermal and chemical denaturation of proteins performed on this dual-modal sensor. Firefly luciferase is a protein that catalyzes luciferin oxidation to emit light in its native state and loses activity if denatured.
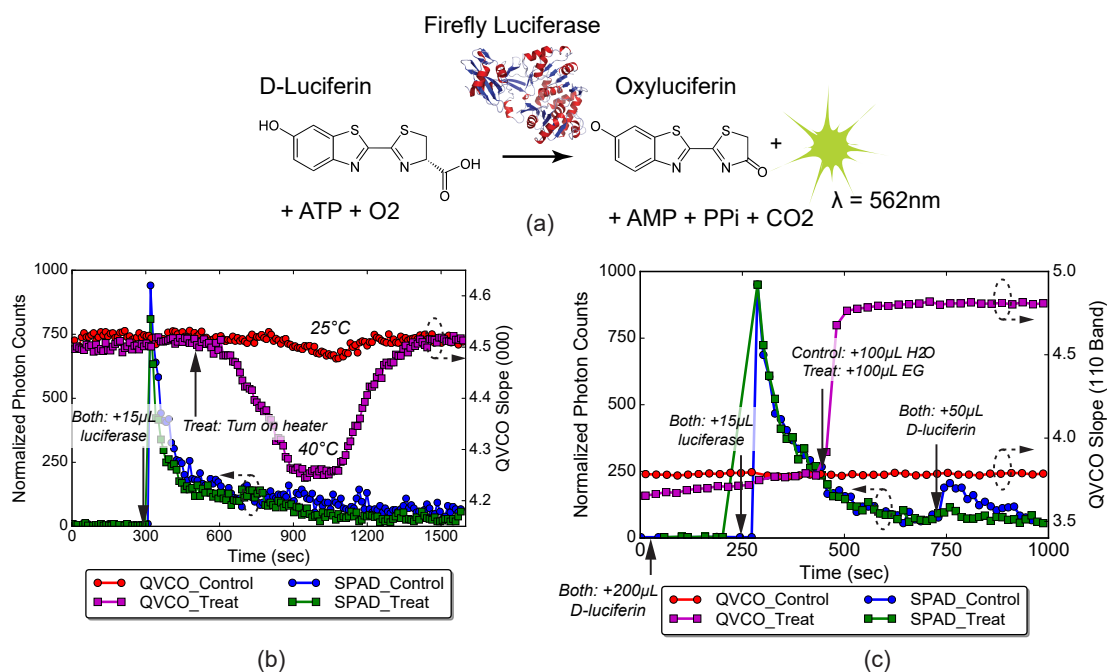
Figure 4.8: Combined microwave and optical measurements of luciferase denaturation due to thermal and chemical stress, (a) reaction formula, (b) luciferase denaturation due to thermal stress and (c) luciferase denaturation due to chemical (ethylene glycol) stress.

In Fig. 4.8(b), the thermal stability of this enzyme is studied. In this experiment, the QVCO is configured as a temperature sensor and the SPADs are used to monitor the activity of luciferase by measuring the intensity of light emission during the luciferaze-catalyzed luminance reaction. When the temperature was increased from 25°C to 40°C at 900s (as

indicated by the purple curve in Fig. 4.8(b)), the light emission decreases slightly faster, indicating a lose of activity in luciferase.

In Fig. 4.8(c), this property is used to study the toxicity of ethylene glycol (EG), a widely-used antifreeze. 250s after luciferin was loaded onto the chip, the reaction was started by adding luciferase and produced a sharp increase in the SPAD photon counts. At 450s, EG was applied and caused an immediate change at the QVCO output. Sufficient time was given for EG to denature luciferase. At 750s, more luciferin was added but only the control group saw an increase in SPAD photon counts, indicating the luciferase was denatured by EG.

Table 4.1 summarizes and compares this work with state of the art[2–5, 8]. A monolithic integration of permittivity sensing at mmWave frequencies and optical sensing at single-photon level is presented, which allows highly sensitive multi-parametric monitoring of biomolecular processes. A novel tank-perturbation based readout scheme is proposed to achieve a reference-and-label-free long-term stability of 5.4ppm with comparable sensitivity and power consumption. As demonstrated by the two experiments, simultaneous optical and microwave sensing provides a better profiling of protein denaturation kinetics and many other complex biomolecular processes.

Table 4.1: System Performance Summary and Comparison

	[2] LoC'18	[3] JSSC'16	[8] JSSC'16	[5] JSSC'18	[4] JSSC'18	**This work**
Technology	130nm CMOS	65nm CMOS	65nm CMOS	110nm CIS	65nm CMOS	**28nm CMOS**
Application	Cell-based assay	Flow cytometry	Biological water	Fluorescence lifetime	Magnetic bead sensing	**Bioreaction monitoring**
Multiparametric?	Yes	No	No	No	No	**Yes**
Label/Reference?	None	Yes	None	Yes	Yes	**None**
Sensor Type	Single electrode (0.5Hz-KHz) / Electrode pair (KHz-MHz) / Photodiode / PTAT thermal	Injection Locked VCO (6.5G-30GHz)	60G/120GHz VCO	Pinned photodiodes	1.4G/3.7GHz transformer-loaded VCO	**QVCO (39-42GHz) / SPAD**
Sensitivity	N.A.	1.25 ppm	2.9/2.7 ppm @120/60G	154** ppm	0.3 ppm	**1.32* ppm**
Long-term Stability (ppm)	N.A.	N.A.	N.A.	N.A.	0.35 (11hr, magnetic label needed)	**5.4* (8hr, label free)**
Sensor Active Area (mm²)	1.152	0.212	0.014/0.008 @120/60G	8.22	0.17	**0.028 8x(30x27)um²**
Power	N.A.	65 mW	35/12 mW @120/60G	600 mW	5 mW	**8.4* mW**

* QVCO-Permittivity sensor specifications
** Calculated based on temporal noise and well capacity

Chapter 5

Conclusion

In conclusion, a fully integrated microwave and optical hybrid biomolecular sensor is analyzed, designed and implemented. The microwave sensing unit is a 37.5G-45.1GHz superharmonic coupled QVCO which is configured to detect the medium permittivity. A novel tank-perturbation based noise-cancellation readout scheme is proposed to achieve label-and-reference-free 5.4ppm long-term stability (in an eight-hour experiment). The optical sensing unit is an array of SPADs (single-photon-avalanche-diodes) for photon counting. It demonstrates first-time implementation in 28nm bulk CMOS, and achieves DCR (dark count rate) of 500/sec and PDE (photon detection efficiency) of 11.5% (520nm) under 1V excessive bias voltage. The two sensors are tested separately with sample liquids for performance characterization. The QVCO-based sensor can measure single-frequency point permittivity as well as liquid dispersion properties for further differentiation. The SPAD-based sensor can perform both photon counting and fluorescence lifetime measurements with around 300ps timing accuracy. An enzyme denaturation experiment is performed to show that multi-parametric sensing provides a better profiling of complex biomolecular processes.

Bibliography

[1] H. Wang, C. Weng, and A. Hajimiri, "Phase noise and fundamental sensitivity of oscillator-based reactance sensors," *IEEE Transactions on Microwave Theory and Techniques*, vol. 61, no. 5, pp. 2215–2229, May 2013.

[2] J. Seok Park *et al.*, "Multi-parametric cell profiling with a CMOS quad-modality cellular interfacing array for label-free fully automated drug screening," *Lab on a Chip*, vol. 18, no. 19, pp. 3037–3050, 2018.

[3] J. Chien and A. M. Niknejad, "Oscillator-based reactance sensors with injection locking for high-throughput flow cytometry using microwave dielectric spectroscopy," *IEEE Journal of Solid-State Circuits*, vol. 51, no. 2, pp. 457–472, Feb. 2016.

[4] C. Sideris, P. P. Khial, and A. Hajimiri, "Design and implementation of reference-free drift-cancelling CMOS magnetic sensors for biosensing applications," *IEEE Journal of Solid-State Circuits*, vol. 53, no. 11, pp. 3065–3075, Nov. 2018.

[5] M. Seo *et al.*, "A time-resolved four-tap lock-in pixel CMOS image sensor for real-time fluorescence lifetime imaging microscopy," *IEEE Journal of Solid-State Circuits*, vol. 53, no. 8, pp. 2319–2330, Aug. 2018.

[6] H. Wang, S. Kosai, C. Sideris, and A. Hajimiri, "An ultrasensitive CMOS magnetic biosensor array with correlated double counting noise suppression," in *2010 IEEE MTT-S International Microwave Symposium*, May 2010, pp. 616–619.

[7] C. Ronne *et al.*, "Investigation of the temperature dependence of dielectric relaxation in liquid water by THz reflection spectroscopy and molecular dynamics simulation," *J. Chem. Phys.*, vol. 107, no. 14, pp. 5319–5331, Oct. 1997.

[8] T. Mitsunaka *et al.*, "CMOS biosensor IC focusing on dielectric relaxations of biological water with 120 and 60 GHz oscillator arrays," *IEEE Journal of Solid-State Circuits*, vol. 51, no. 11, pp. 2534–2544, Nov. 2016.

[9] Y.-T. Liao, H. Yao, A. Lingley, B. Parviz, and B. P. Otis, "A 3-uW CMOS glucose sensor for wireless contact-lens tear glucose monitoring," *IEEE Journal of Solid-State Circuits*, vol. 47, no. 1, pp. 335–344, Jan. 2012.

[10] Y. Hu *et al.*, "3D gesture-sensing system for interactive displays based on extended-range capacitive sensing," in *2014 IEEE International Solid-State Circuits Conference Digest of Technical Papers (ISSCC)*, Feb. 2014, pp. 212–213.

[11] R. Adler, "A study of locking phenomena in oscillators," *Proceedings of the IEEE*, vol. 61, no. 10, pp. 1380–1385, Oct. 1973.

[12] A. Rofougaran, J. Rael, M. Rofougaran, and A. Abidi, "A 900 MHz CMOS LC-oscillator with quadrature outputs," in *1996 IEEE International Solid-State Circuits Conference. Digest of Technical Papers, ISSCC*, Feb. 1996, pp. 392–393.

[13] P. Andreani and X. Wang, "On the phase-noise and phase-error performances of multiphase LC CMOS VCOs," *IEEE Journal of Solid-State Circuits*, vol. 39, no. 11, pp. 1883–1893, Nov. 2004.

[14] N. C. Kuo, J. C. Chien, and A. M. Niknejad, "Design and analysis on bidirectionally and passively coupled QVCO with nonlinear coupler," *IEEE Transactions on Microwave Theory and Techniques*, vol. 63, no. 4, pp. 1130–1141, Apr. 2015.

[15] T. Xi *et al.*, "Low-phase-noise 54-GHz transformer-coupled quadrature VCO and 76-/90-GHz VCOs in 65-nm CMOS," *IEEE Transactions on Microwave Theory and Techniques*, vol. 64, no. 7, pp. 2091–2103, Jul. 2016.

[16] S. L. J. Gierkink, S. Levantino, R. C. Frye, C. Samori, and V. Boccuzzi, "A low-phase-noise 5-GHz CMOS quadrature VCO using superharmonic coupling," *IEEE Journal of Solid-State Circuits*, vol. 38, no. 7, pp. 1148–1154, Jul. 2003.

[17] P. Tortori, D. Guermandi, M. Guermandi, E. Franchi, and A. Gnudi, "Quadrature VCOs based on direct second harmonic locking: theoretical analysis and experimental validation," *Int. J. Circuit Theory Appl.*, vol. 38, no. 10, pp. 1063–1086, Dec. 2010.

[18] A. Hajimiri and T. Lee, "Design issues in CMOS differential LC oscillators," *IEEE Journal of Solid-State Circuits*, vol. 34, no. 5, pp. 717–724, May 1999.

[19] V. Szortyka *et al.*, "A 42mW 230fs-jitter sub-sampling 60 GHz PLL in 40nm CMOS," in *2014 IEEE International Solid-State Circuits Conference Digest of Technical Papers (ISSCC)*, Feb. 2014, pp. 366–367.

[20] X. Yi, C. C. Boon, H. Liu, J. F. Lin, and W. M. Lim, "A 57.9-to-68.3 GHz 24.6 mW frequency synthesizer with in-phase injection-coupled QVCO in 65 nm CMOS technology," *IEEE Journal of Solid-State Circuits*, vol. 49, no. 2, pp. 347–359, Feb. 2014.

[21] A. Mirzaei, M. E. Heidari, R. Bagheri, S. Chehrazi, and A. A. Abidi, "The quadrature LC oscillator: a complete portrait based on injection locking," *IEEE Journal of Solid-State Circuits*, vol. 42, no. 9, pp. 1916–1932, Sep. 2007.

[22] J. J. Rael and A. A. Abidi, "Physical processes of phase noise in differential LC oscillators," in *Proceedings of the IEEE 2000 Custom Integrated Circuits Conference*, May 2000, pp. 569–572.

[23] H. Wey and W. Guggenbuhl, "Noise transfer characteristics of a correlated double sampling circuit," *IEEE Transactions on Circuits and Systems*, vol. 33, no. 10, pp. 1028–1030, Oct. 1986.

[24] S. M. Sze and K. K. Ng, *Physics of semiconductor devices.* John Wiley & Sons, Nov. 2006.

[25] A. Spinelli and A. L. Lacaita, "Physics and numerical simulation of single photon avalanche diodes," *IEEE Transactions on Electron Devices*, vol. 44, no. 11, pp. 1931–1943, Nov. 1997.

[26] A. Vil, A. Arbat, E. Vilella, and A. Dieguez, "Geiger-mode avalanche photodiodes in standard CMOS technologies," *Photodetectors*, Mar. 2012.

[27] I. M. Antolovic *et al.*, "Photon-counting arrays for time-resolved imaging," *Sensors*, vol. 16, no. 7, p. 1005, Jul. 2016.

[28] K. W. Chew, J. Zhang, K. Shao, W. B. Loh, and S. Chu, "Impact of deep N-Well implantation on substrate noise coupling and RF transistor performance for systems-on-a-chip integration," in *32nd European Solid-State Device Research Conference*, Sep. 2002, pp. 251–254.

[29] Q. Pan, Z. Hou, Y. Li, A. W. Poon, and C. P. Yue, "A 0.5-V P-Well/Deep N-Well photodetector in 65-nm CMOS for monolithic 850-nm optical receivers," *IEEE Photonics Technology Letters*, vol. 26, no. 12, pp. 1184–1187, Jun. 2014.

[30] E. Charbon, "Single-photon imaging in complementary metal oxide semiconductor processes," *Philos Trans A Math Phys Eng Sci*, vol. 372, no. 2012, Mar. 2014.

[31] T. C. d. Albuquerque *et al.*, "Integration of SPAD in 28nm FDSOI CMOS technology," in *2018 48th European Solid-State Device Research Conference (ESSDERC)*, Sep. 2018, pp. 82–85.

[32] S. Pellegrini *et al.*, "Industrialised SPAD in 40 nm technology," in *2017 IEEE International Electron Devices Meeting (IEDM)*, Dec. 2017, pp. 16.5.1–16.5.4.

[33] E. Charbon, H. Yoon, and Y. Maruyama, "A Geiger mode APD fabricated in standard 65nm CMOS technology," in *2013 IEEE International Electron Devices Meeting*, Dec. 2013, pp. 27.5.1–27.5.4.

[34] M. A. Karami, H. J. Yoon, and E. Charbon, "Single-photon avalanche diodes in sub-100nm standard CMOS technologies," *Proc. Intl. Image Sensor Workshop (IISW)*, 2011.

[35] Q. S. Hanley, V. Subramaniam, D. J. ArndtJovin, and T. M. Jovin, "Fluorescence lifetime imaging: multi-point calibration, minimum resolvable differences, and artifact suppression," *Cytometry*, vol. 43, no. 4, pp. 248–260, Apr. 2001.